



ANALYSIS OF PORE NETWORKS AND RESERVOIR QUALITY OF THE UPPER CRETACEOUS WOODBINE SANDSTONE IN THE HIGH-RECOVERY-EFFICIENCY, GIANT EAST TEXAS FIELD

Robert G. Loucks, Robert M. Reed, and William A. Ambrose

*Bureau of Economic Geology, Jackson School of Geosciences, University of Texas at Austin,
University Station, Box X, Austin, Texas 78713–8924, U.S.A.*

ABSTRACT

Reservoir quality in the Upper Cretaceous Woodbine sandstone in the giant East Texas Field is excellent and has contributed to the exceptionally high oil-recovery efficiency rate of approximately 77 percent. The sandstone has a stable mineralogy consisting predominantly of quartz with very minor amounts of rock fragments and feldspar, and it also has had a favorable diagenetic history. Primary intergranular pores are the main constituent of the pore network. Porosities within the matrix-free sandstones average 26 percent, and permeabilities average nearly 2000 md based on core analysis.

The Woodbine sandstone is predominantly a fine- to medium-grained quartz arenite with a few samples in the sublitharenite field. Granule to pebble conglomerates are common at the base of incised valleys and are composed of silicified carbonate (chert) and quartzite clasts. The material between the granules and pebbles is medium- to coarse-grained sand composed of quartz and chert. Lower-energy facies contain a clay matrix rich in nano- to micropores.

Quartz overgrowths are the most common cement; from scanning electron microscope cathodoluminescence analysis, the overgrowths appear to have been precipitated in two stages, starting at shallow burial depths of less than 2600 ft. Other cements are relatively rare and include poikilotopic calcite, siderite crystals, and chlorite coats or grain replacement. Intergranular pores between grains are the predominant pore type, and minor secondary dissolution pores are present within feldspars, volcanic rock fragments, and chert. Some of the conglomerates contain micro- to macroporous chert clasts.

Mercury-injection capillary pressure analysis shows that the high-quality sandstones have entry pressures of <6 psi and mean pore-throat sizes between 5 and 15 μm in diameter, whereas one matrix-rich sandstone has an entry pressure of 82 psi and poorly-sorted pore-throat sizes that range between 0.01 and 1 μm in diameter. Overall reservoir quality in the Woodbine sandstone is excellent and not an important risk factor in the exploitation of the East Texas Field.

INTRODUCTION

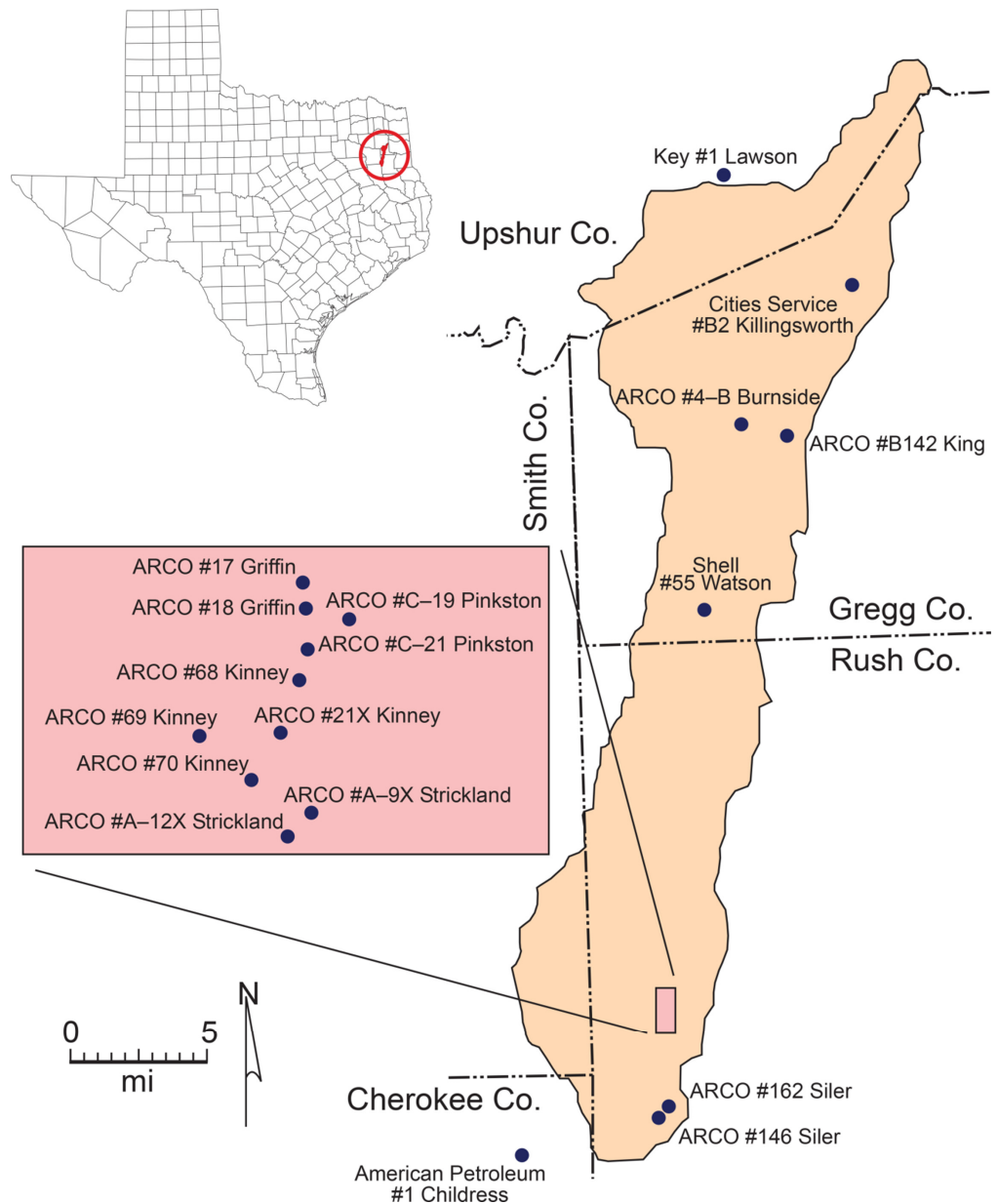
The East Texas Field (Fig. 1) is a giant oil field that has been producing from Upper Cretaceous Woodbine sandstones (Fig. 2) since 1930 (Wang et al., 2008). According to Ambrose and Hentz (2010), this field is the most productive oil field in the lower 48 states. It has produced more than 5.4 billion stock-tank barrels of oil, and it has a recovery efficiency of ~77 percent, highest of any giant oil field in the world (Wang et al., 2008). The exceptional production and high recovery efficiency are related to several factors: (1) large closure (130,144 ac), (2) well-connected sandstone bodies, (3) quartz-rich provenance, (4) high-quality reservoirs (matrix-free sandstones averaging approxi-

mately 2000 md), (5) light oil with a 39° American Petroleum Institute (API) gravity, (6) early field-maintenance pressure program, and (7) close well spacing (averaging 4.2 ac) of over 31,000 wells (Halbouty, 1991; Wang et al., 2008; Ambrose et al., 2010; Hentz, 2010; Loucks, 2010).

Objectives of this paper are to: (1) define the mineralogy, texture, and fabric of the Woodbine sandstone reservoirs in the East Texas Field area; (2) comment on the diagenetic history of the sandstones and conglomerates that led to the preservation of high-quality reservoirs; (3) characterize pore networks using thin sections, scanning electron microscopy (SEM) (including energy-dispersive spectroscopy and cathodoluminescence [SEM-CL] analyses), core analysis, and mercury-injection capillary-pressure (MICP) analysis; and (4) discuss the relationship between reservoir quality and depositional lithofacies.

A few studies have addressed the petrography and reservoir quality of the Woodbine reservoirs (Cotera, 1956; Beall, 1964; Halbouty, 1991; Loucks, 2010). Only Loucks (2010) attempted to integrate lithofacies, petrographic, and petrophysical data to address the origin and occurrence of high-quality reservoirs with-

Figure 1. Map of East Texas Field showing location of core and thin-section data used in this investigation (modified after Loucks, 2010).



in the Woodbine sandstone. This present investigation is an extension of the study done by Loucks (2010). Additional data for the Woodbine sandstone-reservoir-quality study includes petrographic data, new SEM and SEM-CL analyses, in situ core porosity and permeability analyses, and MICP analyses.

DATA AND METHODS

The basic rock data for this investigation on reservoir quality consist of approximately 1600 ft of core from 20 wells. Of these cores, described by Ambrose et al. (2009) and Ambrose and Hentz (2010), 18 were sampled for thin sections (Fig. 1) to define the petrographic and petrophysical controls on reservoir quality. For a representative range of fabrics and textures from different depositional lithofacies, 73 thin sections were selected, including sandstones with and without matrix. Thin sections were stained with amaranth and cobaltinitrite solutions to aid in the recognition of plagioclase and K-feldspar, respectively. All thin sections were impregnated with blue epoxy to observe macropores and with blue fluorescent dye to observe micropores (using UV light). The thin sections were reviewed, and 31 thin sections

were point counted. To ensure that the whole thin section was analyzed, 200 to 250 points were counted per thin section in four major categories: (1) detrital framework grains, (2) matrix, (3) authigenic cements, and (4) pores. Framework grains include quartz, feldspars, and rock fragments; chert is treated as a rock fragment. Grains such as biotite and muscovite were counted but not included in the calculation of framework. Grain size was estimated by measuring a sampling of grains and sorting was estimated from standard sorting diagrams.

Most of the cathodoluminescence photomicrographs used in this investigation were produced using an Oxford Instruments Mono-CL detector and PA-3 amplifier attached to an FEI XL-30 SEM. Other SEM photomicrographs were produced using a Gatan ChromaCL system attached to an FEI Nova NanoSEM 430. These systems use a retractable parabolic mirror and a photomultiplier tube to collect and amplify luminescence (Kearsley and Wright, 1988). Color CL images from the Oxford MonoCL system were obtained by combining three grayscale images produced using red, green, and blue filters. Signal amplification during CL image acquisition was selected to obtain maximum contrast and signal-to-noise ratio. Contrast and saturation were

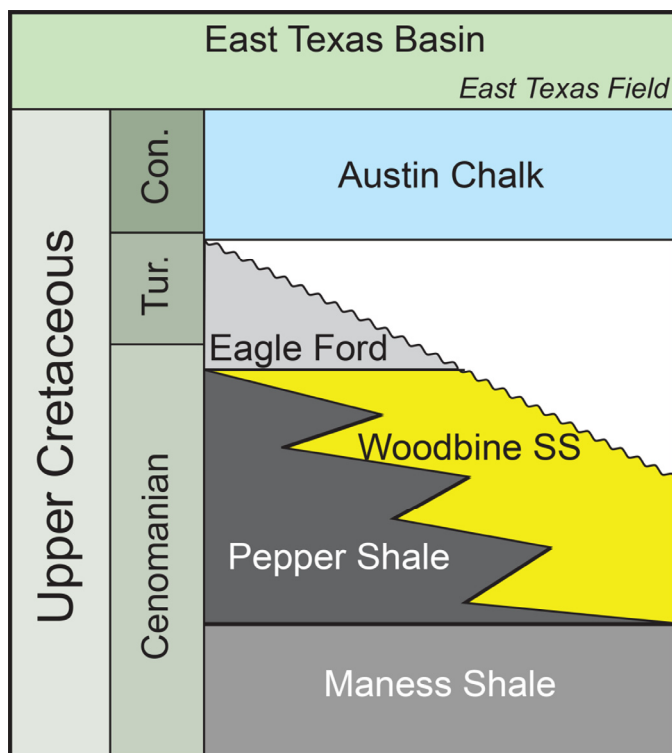


Figure 2. Stratigraphic section in the area of the East Texas Field in the East Texas Basin.

further enhanced during digital image processing. The SEM was operated at 12–15 kV. The spot size (sample current) used for CL imaging was larger than that typically used for secondary electron imaging on an SEM and was more typical of the settings recommended for EDS mapping (setting 6.3 on the XL-30 and 5.0 on the Nova NanoSEM). Samples were positioned 1 to 1.5 mm beneath the bottom of the CL mirror assembly. Samples discussed here are polished thin sections coated with a layer of carbon 25 to 30 nm in thickness.

Phase identification and elemental mapping were conducted with two different energy dispersive spectroscopy (EDS) systems. Early work was done with an Oxford Instruments ISIS system; later work was done with dual Bruker XFlash[®] SDD systems. Broad-ion-beam milling with Ar-ions was performed using a Leica EM Triple Ion-Beam Cutter 020 (TIC020) on two samples to investigate nano- and micropores in the matrix. Samples were milled using an accelerating voltage of 8 kV, a source current of 2.8 mA, and a milling time of 10 hr. Ion-milled samples received a 4 to 6 nm coating of Ir to prevent charging.

Core Laboratories (Houston, Texas) performed MICP analysis on five sandstone samples. The sandstones were subjected to an injection pressure of 55,000 psi to ensure that micropore-throat diameters as small as 0.01 μm were measured.

REGIONAL SETTING, SOURCE AREAS, AND DEPOSITIONAL FACIES

The regional setting, sequence stratigraphy, stratal architecture, and lithofacies of the Woodbine Group has been presented by Ambrose et al. (2009), Ambrose and Hentz (2010), and Hentz and Bonnaffé (2010). The deposition setting of the East Texas Field Woodbine sediments (gravels, sands, and muds) was in the East Texas Basin (Fig. 1) on the drowned Upper Cretaceous shelf before the rise of the Sabine Uplift. The Woodbine section overlies the Cenomanian Buda Limestone and erosionally underlies the Coniacian Austin Chalk (Fig. 2).

According to Hentz and Bonnaffé (2010), 14 fourth-order sequences compose the Woodbine Group in the deeper part of the East Texas Basin to the west. In the area of the East Texas Field, only the lowermost fourth-order sequences remain. Much of the upper section was eroded during the rise of the Sabine Uplift. Ambrose et al. (2009) and Ambrose and Hentz (2010) interpreted that two major systems tracts comprise the Woodbine section: (1) a highstand fluvial-dominated deltaic system and (2) a lowstand incised-valley fluvial system. See Ambrose et al. (2009) and Ambrose and Hentz (2010) for a detailed description and discussion of the two systems tracts. Depositional processes within each systems tract controlled the characteristics and distribution of the sediment within them. In general, the lowstand incised-valley fluvial system deposited coarser sediment (sand and gravel) than did the highstand fluvial-dominated deltaic system (sand). The sandstones in the lowstand incised-valley fluvial system are generally thicker and more widespread. An example of a core and associated core slabs and thin sections from each systems tract is shown in Figures 3 and 4 to demonstrate the stacking patterns, lithofacies types, and texture and fabric of the Woodbine strata.

On the basis of abundant plutonic-type quartz, Cotera (1956), Beall (1964), and Oliver (1971) each agreed that a major sediment source was from the Mid-Continent area to the north and northeast in the area of the Ouachita Mountains (Fig. 5). Based on sandstone-percent maps, Sims (1982) also agreed that a major source of sand was from the Mid-Continent area. Cotera (1956) and Oliver (1971) suggested that some of the Woodbine sediments, especially metaquartz, were sourced from igneous Precambrian and Paleozoic rocks in the Appalachian orogenic belt, but Beall (1964) concluded that if the Appalachian were a source of sediment, this source was insignificant. Beall (1964) suggested that all the metaquartz could be attributed to the Ouachita source area. The volcanic rock fragments are interpreted to be sourced from the Arkansas area (Fig. 5), where Late Cretaceous volcanism took place (Cotera, 1956). Cotera (1956) described the volcanic rock fragments as being eroded from ultrabasic volcanic outcrops and cited Ross et al. (1929) as documenting Late Cretaceous volcanic activity in southwestern Arkansas.

PETROGRAPHY

The Woodbine sandstones in the East Texas Field have a wide range of fabrics, depending on in which sequence systems tract they occur and in what depositional environment within the systems tract they were deposited. As noted by Ambrose et al. (2009) and Ambrose and Hentz (2010), the lowstand incised-valley fill contains an assortment of fabrics including sandy chert conglomerates, sandstones, and mudstones (Fig. 4), whereas the highstand deltaic systems tract has generally only sandstones and mudstones (Fig. 3). Sandstones in both systems tracts consist of very fine- to medium-grained sand. The granule to pebble conglomerates contain a matrix of medium- to coarse-grained sand. Silt- and clay-matrix-rich sandstones are common in both systems tracts.

Matrix-Free Sandstone

Based on point-count data, the Woodbine sandstone is predominantly a quartzarenite (>95% framework quartz) with a few samples in the sublitharenite field using the classification of Folk (1974) (Fig. 6). Therefore, quartz grains are the major constituent (Fig. 7). Other framework grains include chert and rare feldspar (plagioclase and K-feldspar), volcanic rock fragments, and mud clasts (Fig. 8). Mud clasts were soft and ductile, were readily compacted, and formed pseudomatrix during compaction (Fig. 8F). Other grains recognized are siltstone fragments, muscovite, biotite, and opaques. Quartz grains are of two major types: plu-

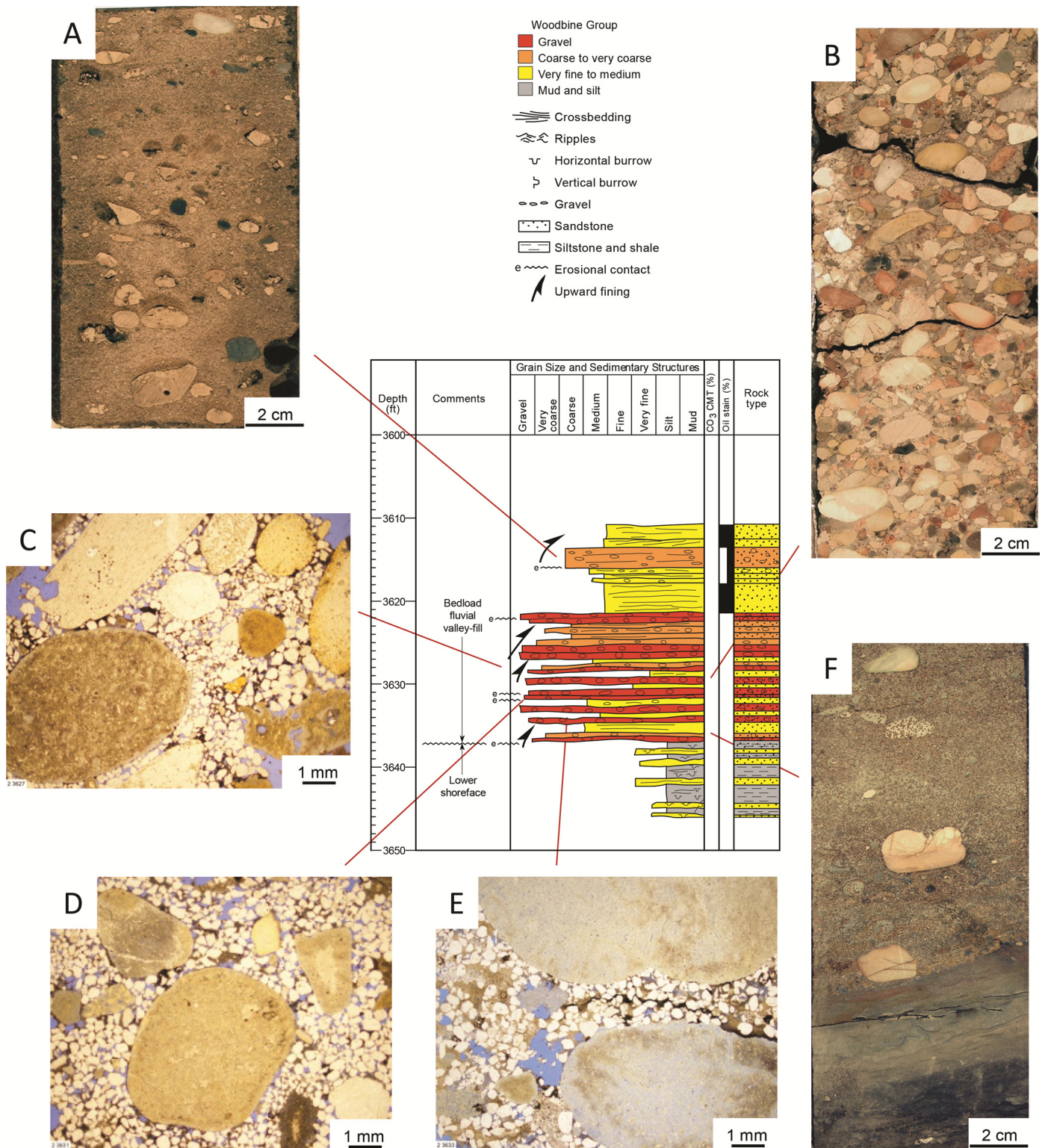


Figure 3. Core description, core slabs, and thin sections from the Cities Service No. B2 Killingsworth well. See Figure 1 for location. Examples of sedimentation in fluvial systems in a lowstand incised valley. (A) Pebble-rich, coarse-grained sandstone (3614 ft). (B) Sandy conglomerate (3629 ft). (C) Sandy conglomerate with chert granules and pebbles (3627 ft). (D) Granule-rich medium- to coarse-grained sandstone (3631 ft). Clasts are chert. (E) Granule-rich medium- to coarse-grained sandstone (3634 ft). Clasts are chert. (F) Very fine-grained sandstone overlain by chert-pebble-rich medium- to coarse-grained sandstone (3636 ft). Core description and depositional environment interpretations are from Ambrose and Hentz (2010).

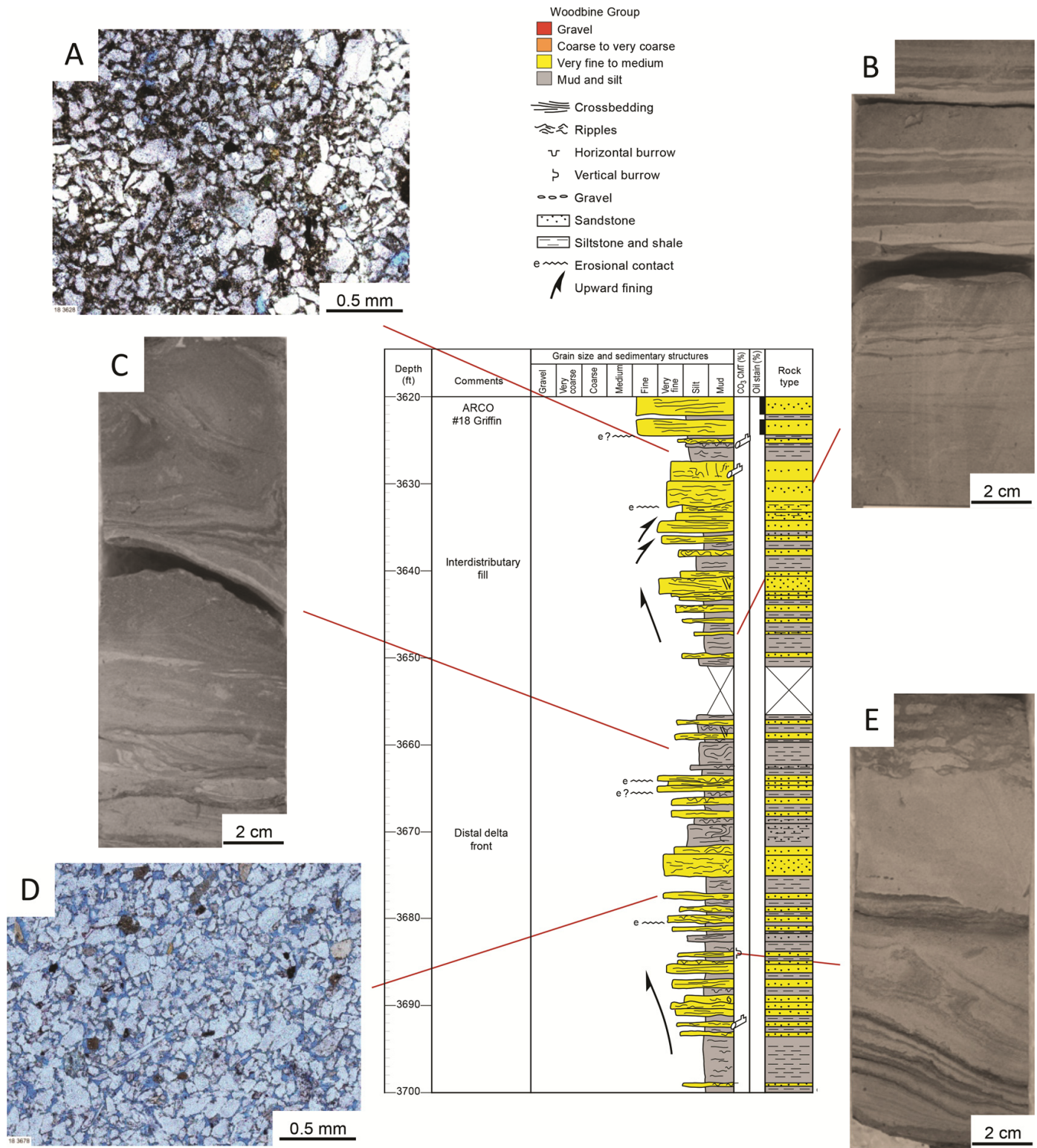


Figure 4. Core description, core slabs, and thin sections from the ARCO No. 18 Griffin well. See Figure 1 for location. Examples of sedimentation in deltaic systems in a highstand systems tract. (A) Very fine-grained, matrix-rich sandstone (3628 ft). (B) Poorly-bedded, very fine-grained sandstone deposited in a delta front environment (3657 ft). (C) Convoluted-bedded, very fine-grained sandstone deposited in a distal delta front environment (3661 ft). (D) Very fine-grained, matrix-free sandstone (3678 ft). (E) Convoluted-bedded, very fine-grained sandstone deposited in a proximal delta front environment (3683 ft). Core description and depositional environment interpretations are from Ambrose and Hentz (2010).

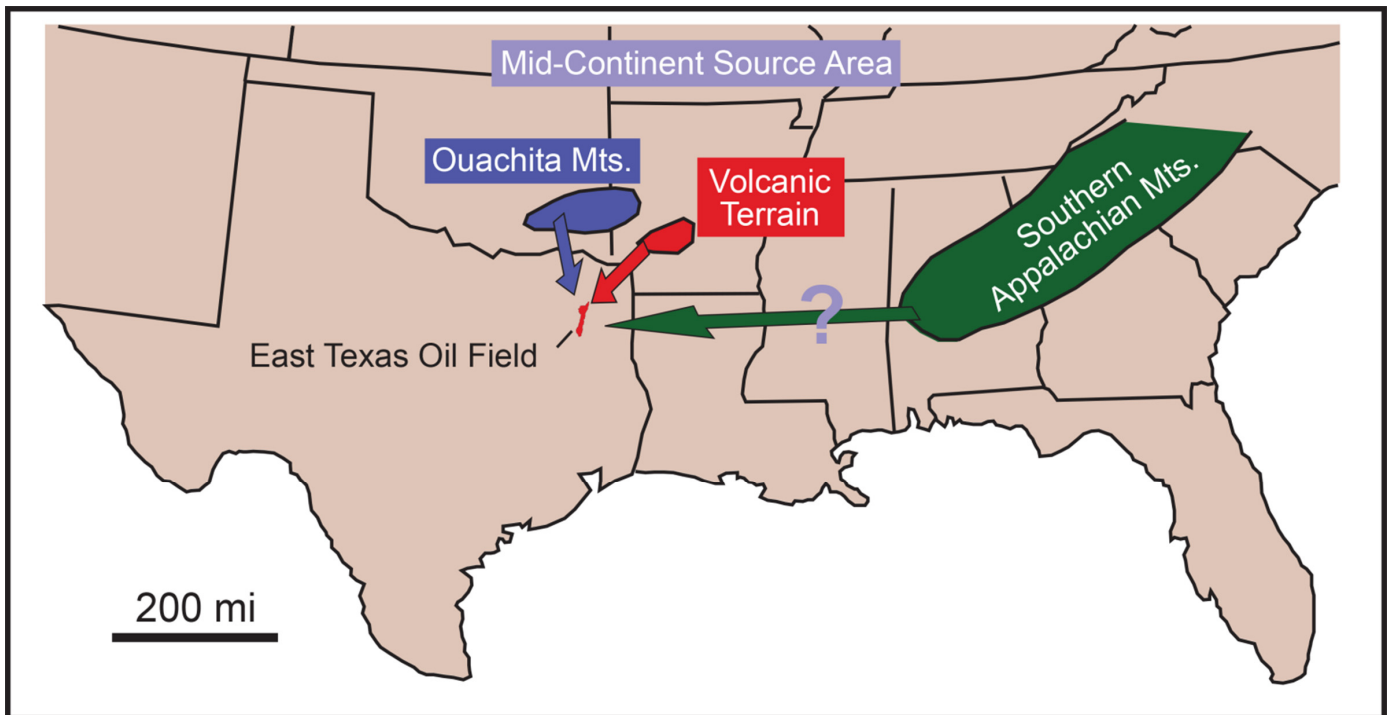


Figure 5. Suggested source areas for Woodbine sandstones in the East Texas Field area (modified after Cotera [1956] and Loucks [2010]).

tonic (common) quartz (Figs. 7A and 7B) and metaquartz (Fig. 7C). Feldspar includes plagioclase, K-feldspar, and microcline. Many of the feldspar grains have been dissolved (Fig. 8A and 8B) or sericitized. Rare volcanic rock fragments show clay replacement or partial dissolution (Figs. 8C and 8D). SEM-CL imaging is necessary to identify the true shapes and sizes of the quartz grains because the majority of the grains do not have dust or bubble rims outlining their actual shapes. Figures 7D–7F documents the actual shapes and sizes of the quartz sand grains using SEM-CL microscopy. Some of the quartz grains have very irregular shapes and some contain quartz-cemented fractures inherited from the source area (Figs 7D and 7E).

Matrix-Rich Sandstone

Lower-energy facies contain a silty and mixed smectite/illite clay matrix according to Beall (1964). The matrix-rich sandstones appear to contain slightly more feldspar, especially K-feldspar, than the matrix-free sandstones, which may be the result of less dissolution of feldspars in matrix-rich sandstones or because the feldspars in the higher-energy deposited sands were eliminated by mechanical abrasion. In some matrix-rich sandstones, the mud matrix occludes all pores, whereas in other matrix-rich sandstones not all pores are totally occluded (Figs. 9A and 9B). This is an important observation because the sandstones where some pores are not occluded still retain moderate permeability, a fact discussed in the section on reservoir quality.

In thin section, the matrix appears to be composed of silt, clay platelets, and peloids (Fig. 9C); therefore, it is a mud matrix (composed of clay- and silt-sized grains) and not a clay matrix. SEM-CL photomicrographs of the silt grains show that the grains have been previously fractured, cemented with quartz, and then transported to the study area (Fig. 9D). The SEM-CL photomicrographs also show what may be relict eroded quartz overgrowths (Fig. 9D). These relict overgrowths signify that the grains were eroded from older quartz-cemented sandstones.

SEM microphotographs of mud-matrix-rich sandstones show a grain-supported framework creating compaction shadows

where clay platelets are relatively noncompacted (Fig. 9E). The clay platelets are 1 to 5 μm long and 0.5 to 1 μm wide, and have interparticle pores between and within them (Figs. 9E and 9F). Many of the clay platelets show curvature related to minor compaction (Figs. 9E and 9F). Also seen in SEM microphotographs are pyrite framboids showing dissolution, which could be either post coring or related to soil-zone processes during the erosion of the Woodbine section. The authors have seen pyrite framboids undergo dissolution diagenesis both on outcrop and in cores stored for long periods of time.

Granule to Pebble Conglomerate

Granule to pebble conglomerates, common at the base of incised valleys, are composed of quartz pebbles and silicified fossiliferous carbonate pebbles (now chert) (Fig. 10). The material between the granules and pebbles are medium- to coarse-grained sand composed of quartz and chert. Some of the chert is porous, containing micro- to mesopores (Figs. 10B and 10F). The pores in the chert are the result of dissolution of dolomite crystals, sponge spicules, and fine carbonate fragments (Figs. 10C, 10D, and 10F). Some quartzite pebbles are also present (Fig. 10A).

DIAGENESIS PROCESSES AND PRODUCTS

The diagenesis of Woodbine quartzarenites and sublitharenites in the East Texas Field is relatively simple. The two major processes responsible for porosity loss were mechanical compaction and quartz cementation. The amounts of mechanical compaction and quartz cementation were variable, but the composite diagenetic history allowed high-porosity sandstones to be preserved. These two diagenesis processes and other rare cements are discussed in the following sections.

Mechanical Compaction

With burial, unlithified sand compacts and loses porosity. Initial porosity at the surface ranges from 47 to 49 percent

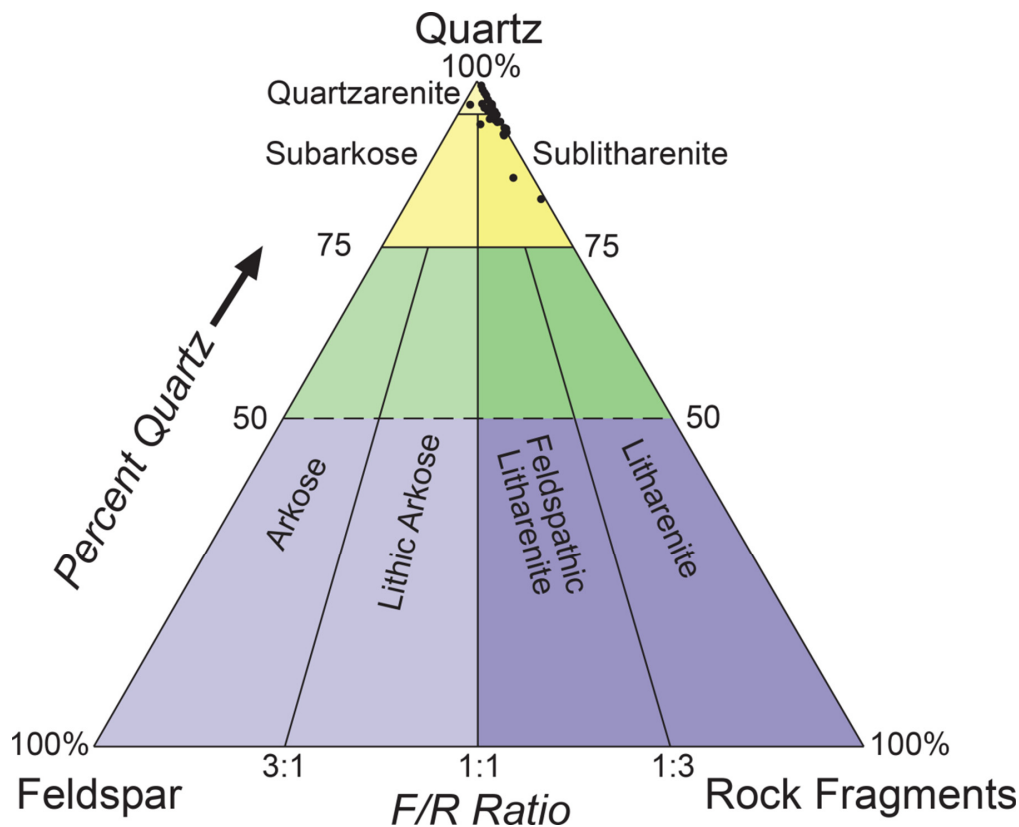


Figure 6. Framework mineralogy plotted on the Folk (1974) ternary diagram. Sandstones plot within the quartzarenite to sublitharenite fields (modified after Loucks, 2010). The majority of rock fragments are chert grains.

(Atkins and McBride, 1992) in sands similar to those deposited in the Woodbine nearshore and fluvial environments. Paxton et al. (2002) calculated that the maximum amount of porosity that can be lost by compaction in sands starting with approximately 40 percent porosity (Fig. 11) and composed of rigid grains is about 14 percent. The final compaction-related intergranular pore volume (IGV) would ideally be 26 percent. See Houseknecht (1987), Lundegard (1992), Ehrenberg (1995), and Paxton et al. (2002) for in-depth discussions of IGV. The mean IGV of matrix-free Woodbine sandstones (calculated by point-counting thin sections on a petrographic microscope) is near the maximum derived by Paxton et al. (2002). The mean IGV value is 25.9 percent, which suggests that the Woodbine sand compacted to its maximum; however, the IGV values of these sandstones range from 19 to 34 percent, indicating that grain compaction was arrested at different depths. Burial-history analysis completed for this study permits the conclusion that the Woodbine sandstones were not buried deeper than 6000 ft (approximately 2500 ft deeper than they are buried today). This maximum burial depth would have allowed the Woodbine sand to reach maximum mechanical compaction unless cementation arrested compaction at a shallower depth.

However, another set of data disputes the thin-section-based IGV calculations. Six samples from three cores were imaged by SEM-CL and the images point counted for IGV (Table 1). The samples were selected from those that showed higher quartz cementation (mean of samples selected = 26.8 percent) in thin sections because we thought that the higher amount of quartz cementation would correspond to the sands that cemented the earliest, which would provide an estimate for the most shallow initiation of quartz cementation and framework stabilization. This SEM-CL method allows an accurate calculation of the number of framework grains and cements, especially quartz overgrowths, which are difficult to define in thin sections. From these SEM-CL analyses, IGV's can be calculated with confidence; however, the area of the sample investigated is limited. Five single SEM-CL photomicrographs (area of observation, 0.3 square mm to

0.5 square mm) and a composite set of 15 SEM-CL photomicrographs (area of observation, 4.5 square mm) were analyzed. The single SEM-CL photomicrographs only sampled 15 to 50 sand grains, depending on grain size. The composite SEM-CL image mosaic is estimated to have sampled approximately 600 to 800 sand grains. Two of these SEM-CL examples are shown in Figures 7D and 7E.

Figure 7E is an example of an SEM-CL photomicrograph that was used to calculate IGV. The photomicrograph clearly shows the differentiation between bright luminescent quartz grains and dark nonluminescent quartz cements. (The diagenesis of this sample is discussed in the section on quartz cementation). This small area of the thin-section sample has a high IGV of 39 percent, suggesting that the sand only lost 8 to 10 percent porosity units before cementation initiated, assuming initial porosities from 47 to 49 percent (Atkins and McBride, 1992), which would correspond to approximately 1200 ft of burial according to a modified Paxton et al. (2002) IGV compaction plot. According to the original compaction plot by Paxton et al. (2002), this sand would have to have been subjected to cementation at the surface (Fig. 11). There is no evidence that the quartz cementation is related to surface diagenetic processes. In the six SEM-CL photomicrographs analyzed, IGV has a mean of 41.6 percent with a range of 39.0 to 44.4 percent (Table 1). These IGV analyses support the conclusion that the Woodbine sands in the East Texas Field area started to be stabilized by quartz cement at a shallow depth of burial.

We recognized that identifying quartz overgrowths within Woodbine sandstones under the optical microscope is difficult if dust or bubble rims (Fig. 12A) are not present between the detrital quartz grain and the overgrowth. Because these rims are not common, other criteria were developed to help recognize quartz overgrowths. One criterion is concave/convex boundaries between quartz grains (Figs. 12C and 12D). These boundaries indicate competitive quartz overgrowth cementation, as seen with CL imaging. Also, planar boundaries (Figs. 12E and 12F) between these grains suggest competitive growth between quartz

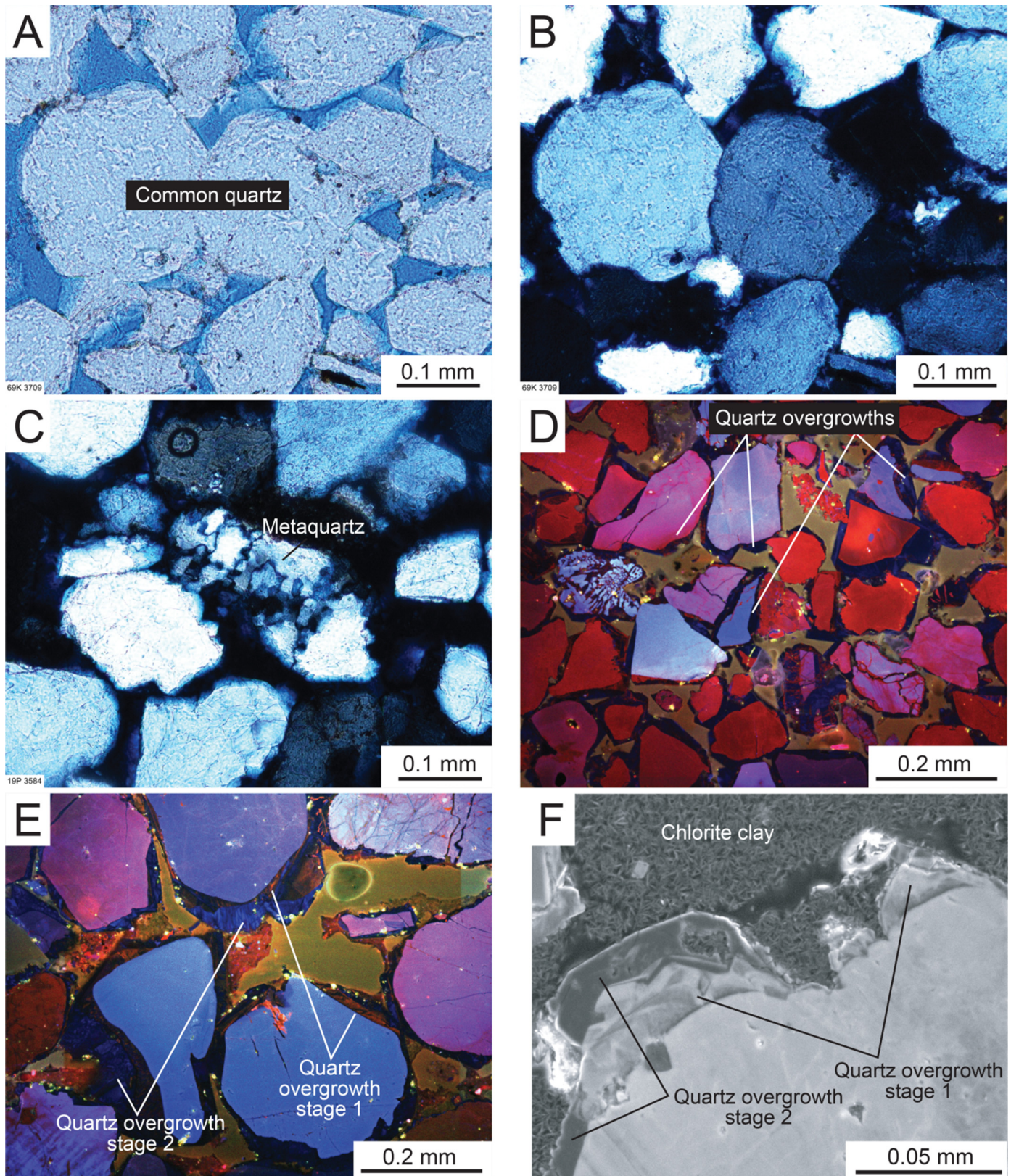


Figure 7. Quartz grains. (A) Very fine- to fine-grained, matrix-free sandstone with some well-developed quartz overgrowths (ARCO No. 69 Kinney; 3709 ft). All grains are common quartz. (B) Same as A, but under cross-polarized light. (C) Very fine- to fine-grained, matrix-free sandstone (ARCO No. C19 Pinkston; 3584 ft). Contains a medium-grained fragment of metaquartz. (D) SEM-CL image of a very fine- to fine-grained, matrix-free sandstone (ARCO No. 68 Kinney; 3627 ft). The CL image shows several stages of quartz overgrowths and that some grains have microfractures inherited from the source area. (E) SEM-CL image of a fine- to medium-grained, matrix-free sandstone (Cities Service No. 2B Killingsworth; 3636 ft). Shows several stages of quartz overgrowths. (F) SEM-CL (red wavelengths) image shows complex internal growth stages of the quartz overgrowths. Note the chlorite-clay-filled pore area within second-stage overgrowth (Cities Service No. 2B Killingsworth; 3637.5 ft).

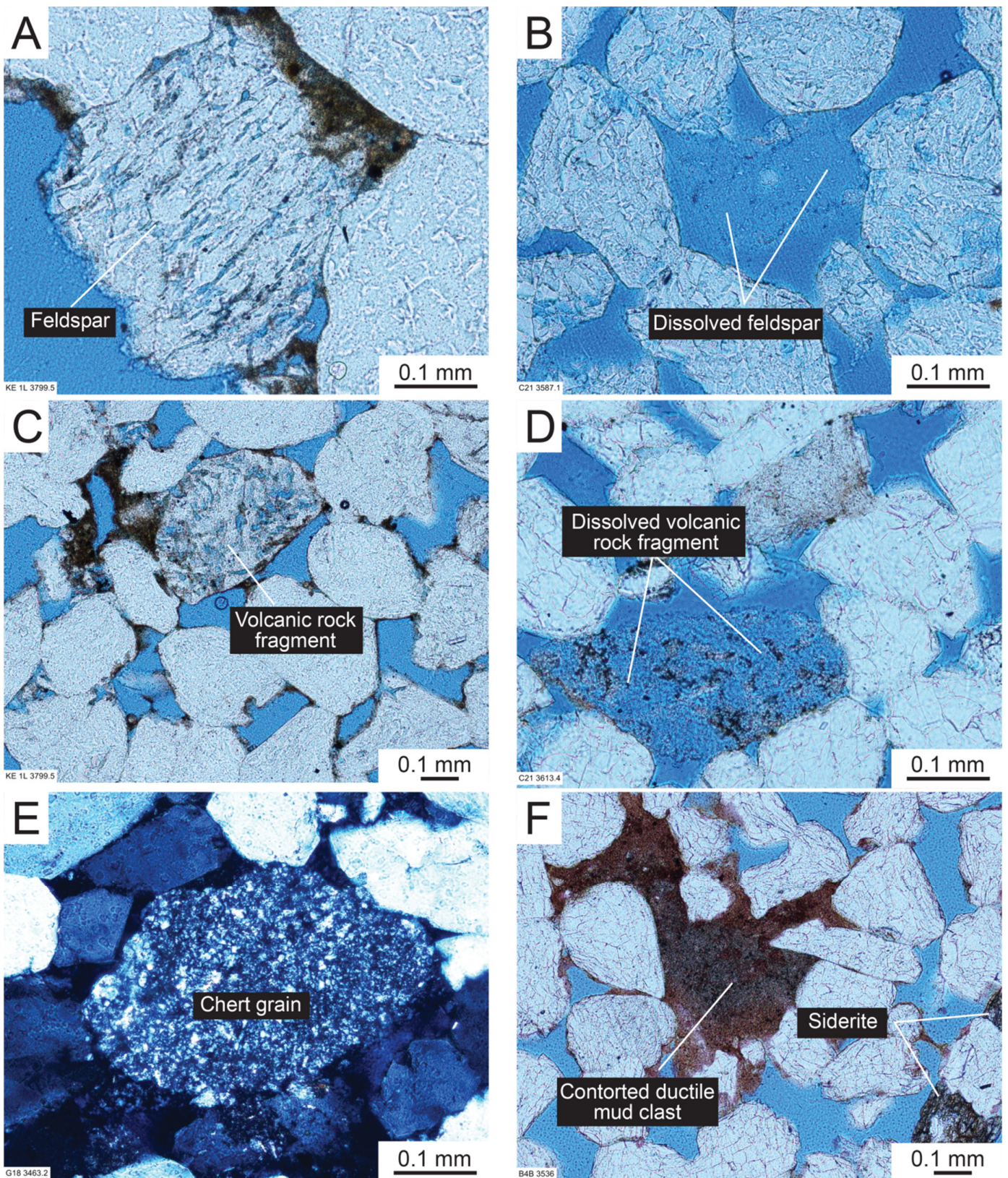


Figure 8. Other grain types. (A) Feldspar grain showing dissolution along cleavage (Key No. 1 Lawson; 3799 ft). (B) Remnants of a dissolved feldspar (ARCO No. C21 Pinkston; 3587.1 ft). (C) Volcanic rock fragment showing partial dissolution (Key No. 1 Lawson; 3799.5 ft). Contains a medium-grained fragment of metaquartz. (D) Remnants of a dissolved volcanic rock fragment (ARCO No. C21 Pinkston; 3613.4 ft). (E) Chert grain under cross-polarized light (ARCO No. 18 Griffin; 3463.2 ft). (F) Compacted ductile mud clast (Key No. 1 Lawson; 3836 ft).

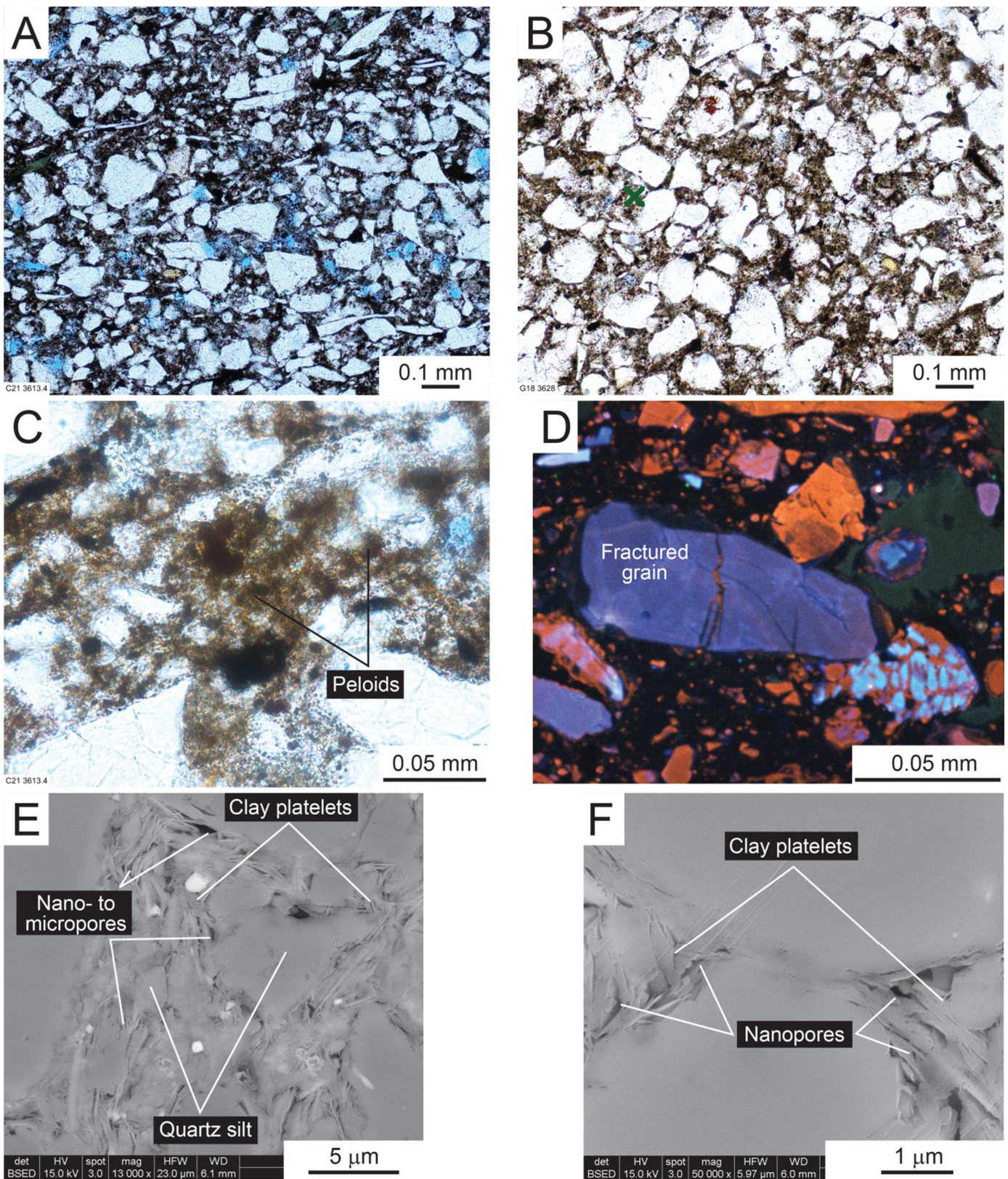


Figure 9. Matrix-bearing sandstones. (A) Matrix-poor sandstone with preserved primary and secondary pores (ARCO No. C21 Pinkston; 3613 ft). (B) Matrix-rich sandstone without macropores (ARCO No. 18 Griffin; 3628 ft). (C) Close-up of matrix composed of quartz silt and clay peloids (ARCO No. C21 Pinkston; 3613 ft). (D) SEM-CL image showing predominantly silt grains in matrix (Cities Service No. B2 Killingsworth; 3637 ft). Some grains have inherited quartz-filled fractures. (E) SEM backscattered electron image showing area between a rigid grain framework (compaction shadow) with clay platelets and silt grains (ARCO No. 18 Griffin; 3628 ft). Nano- and micropores between and within clay platelets. (F) Clay platelets compacted between two quartz grains (ARCO No. 18 Griffin; 3628 ft).

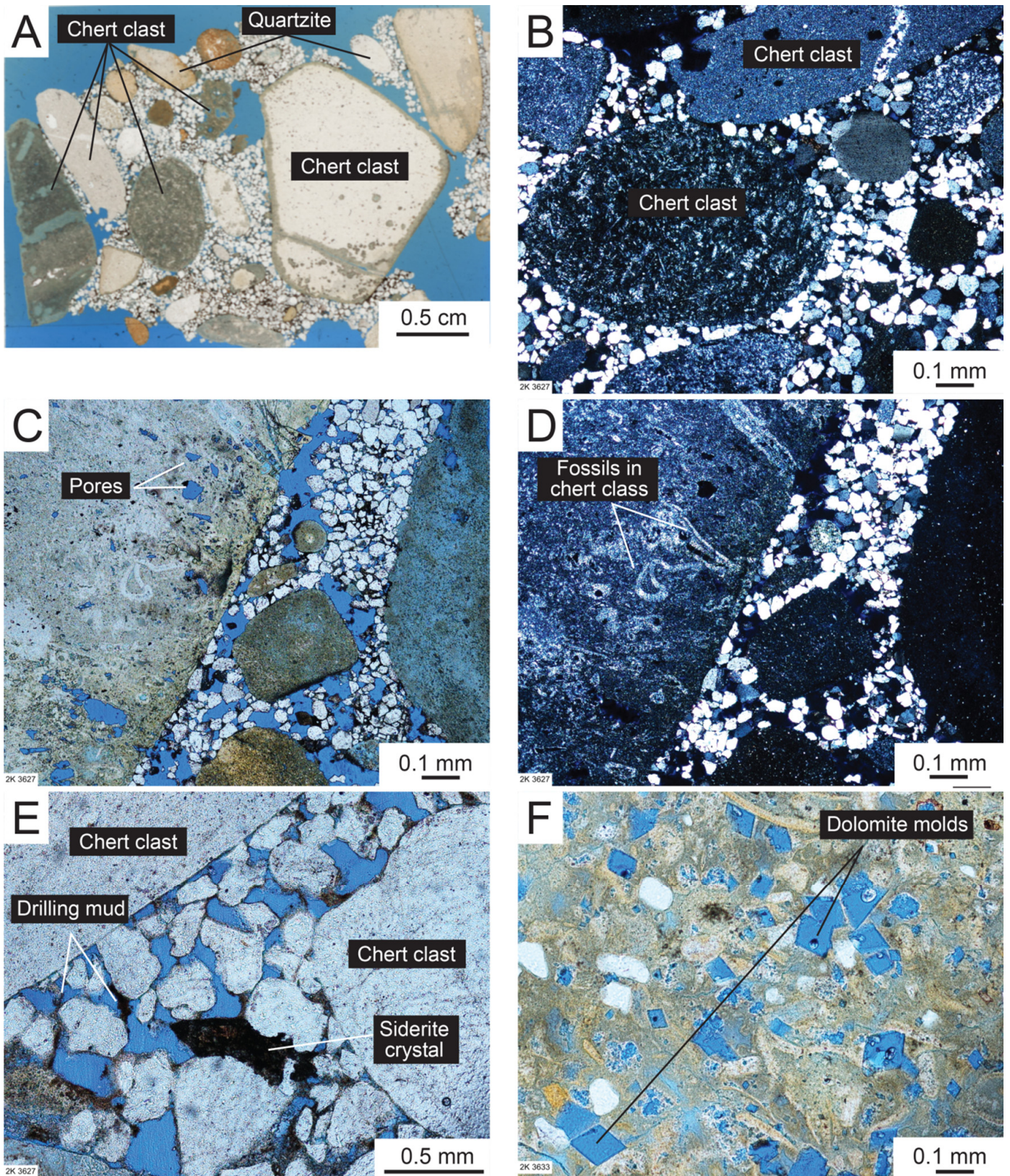


Figure 10. Conglomerate. (A) Sandy conglomerate with rounded chert clasts (Cities Service No. B2 Killingsworth; 3613 ft). (B) Sandy conglomerate with rounded chert clasts (Cities Service No. B2 Killingsworth; 3627 ft). Photomicrograph taken under cross-polarized light. (C) Sandy conglomerate with rounded chert clasts (Cities Service No. B2 Killingsworth; 3627 ft). Chert is silica-replaced fossiliferous limestone. Some dissolution pores are present. (D) Same as C but under cross-polarized light. (E) Area between clasts filled with medium- to coarse-grained sand (Cities Service No. B2 Killingsworth; 3627 ft). Some siderite crystals are present. (F) Chert clast showing dissolved dolomite crystals and scattered micropores (Cities Service No. B2 Killingsworth; 3627 ft).

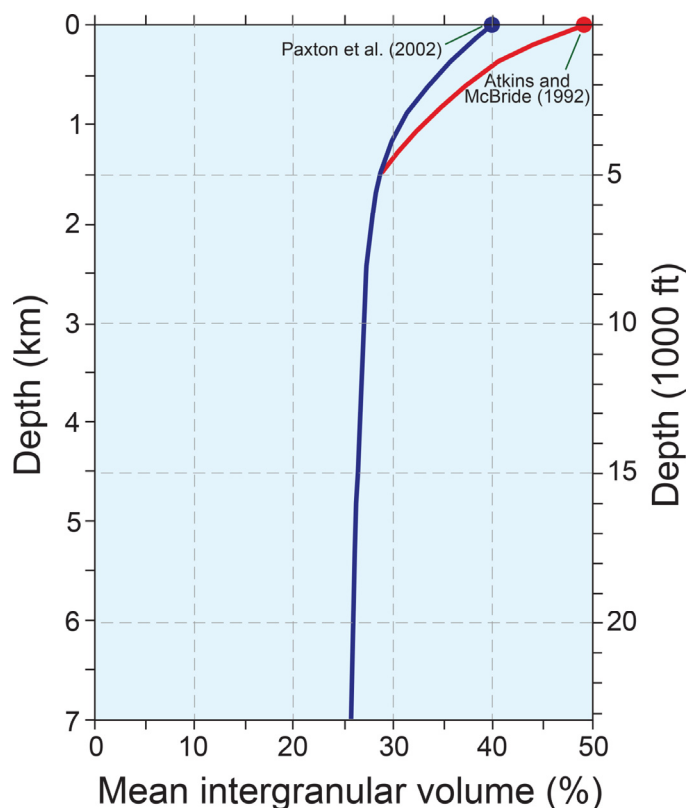


Figure 11. Intergranular volume compaction curve modified from Paxton et al. (2002) for relatively noncemented sand with a rigid-grain framework. The blue line is the compaction curve from Paxton et al. (2002) where the sand at the surface has an initial porosity of approximately 40%. The red curve is a modification of the Paxton et al. (2002) curve using a surface porosity of approximately 48 percent as calculated from Atkins and McBride (1992).

overgrowths, again supported by CL imaging. However, the latter two criteria are not exact and potentially can lead to over- or undercounting quartz overgrowths. Undercounting quartz overgrowths will lead to anomalously low IGV's. Another potential error with point-count-derived IGV's from the optical microscope is that totally-dissolved feldspars and volcanic rock fragments could produce an oversize pore that is counted as an interparticle pore. However, we did not see any dissolved grains that did not leave a partial remnant of the original grain.

The data obtained from thin-section point counts and SEM-CL photomicrograph point counts do not support each other for understanding the IGV of the Woodbine sandstones. The thin-section-based data indicates an IGV mean of 25.9 percent, with a range from 19 to 34 percent and most values between 21 and 27 percent; the SEM-CL photomicrographs provide an IGV mean of 41.6 percent with a range from 39 to 44.4 percent. Through comparing our optical microscope point-count-derived IGV's to the SEM-CL-derived IGV's for the same samples, we have concluded that the SEM-CL-derived IGV's are more reliable and that we most likely undercounted quartz overgrowths with the thin-section point-count method (discussed in the "Quartz Cementation" section below). Therefore, compaction-related porosity loss in the East Texas Woodbine sandstone was low (on the average, less than 10 percent), which is a positive factor leading to high-quality reservoirs.

Cementation

Cementation in the East Texas Woodbine sandstones investigated has a simple history. Quartz is the dominant cement, with

rare carbonate and other cements occurring in a few wells. SEM microscopy also has shown one conglomeratic sandstone with chlorite-clay grain replacement.

Quartz Cementation

Quartz overgrowths are extremely abundant, but where they make contact with the host quartz grains is commonly difficult to define. Therefore, without SEM-CL image analysis, it is not possible to derive accurate percentages for the amount of quartz-overgrowth cement. Thin-section point counts provided a mean value of 8.6 percent for quartz cementation based on a sample population of 21 matrix-free sandstones, but SEM-CL image analysis showed a mean value of 26.8 percent (range of 23.3 to 29.8 percent) for six matrix-free sandstones. Point-count and SEM-CL image-analysis value pairs are presented in Table 1. Table 1 indicates that there is a 100 percent average difference between the amount of quartz overgrowths identified by the two methods and that the SEM-CL identified much-higher percentages of quartz cement. This leads us to conclude that the thin-section point-counting method cannot delineate the amount of quartz overgrowths and that the amount derived by this method is an erroneously low. The original grain (i.e., Fig. 7E) is too irregular to estimate where the quartz overgrowths make contact with the framework quartz grain.

Quartz overgrowths are responsible for the rigid framework of the Woodbine sandstones. In nearly all the wells in this study, quartz overgrowths are the only cement present. Some of the overgrowths have well-developed crystal termination (Fig. 12A), whereas many of the overgrowths do not display apparent crystal facies (Fig. 12B). The quartz overgrowths display competitive cementation as noted by convex/concave (Figs. 12C and 12D) and planar (Figs. 12E and 12F) boundaries. SEM-CL image analysis shows that these are competitive rather than sutured pressure-solution contacts (Figs. 7D and 7E).

Even though the IGV estimates by the thin-section point-count method are unreliable, it is clear that the most realistic values of IGV's are between 35 and 40 percent. IGV's in this range indicate that quartz cementation started at a fairly shallow depth. Based on Paxton et al. (2002), an initial porosity value of sand at the surface of approximately 40 percent would suggest that the initiation of quartz cementation began at a depth shallower than 1400 ft (Fig. 11). However, if we assume that the initial porosity of sand was approximately 48 percent, as suggested by Atkins and McBride (1992), then the range of burial could extend to approximately 2600 ft before the sand started to stabilize (Fig. 11). As will be discussed later, an IGV of 52 percent was calculated in an early pyrite nodule that inhibited compaction. This would support an initial sand porosity higher than that suggested by Paxton et al. (2002) and support the initial sand porosity calculated by Atkins and McBride (1992). In either case, compaction of the Woodbine sands started to be arrested at relatively shallow burial depths while the sands still had porosity values in the range of 35 to 40 percent.

It is interesting to note that Dutton and Land (1988) and Dutton and Diggs (1990), based on $\delta^{18}\text{O}$ isotope analysis, calculated that quartz cements were precipitated in the Lower Cretaceous Travis Peak Formation in East Texas between the temperatures of 131 to 167°F at depths of 3000 to 4500 ft. The cooler temperature range for the initiation of quartz cementation fits well with what is calculated for the Woodbine sandstones in the East Texas Field based on IGV analysis.

Based on burial-history analysis, the Woodbine sandstones in the East Texas Field area were buried to approximately 6000 ft following the initial stage of quartz cementation. Quartz precipitation would have continued through this extended depth range. Later uplift and erosion of the area during early Tertiary time resulted in the strata arriving at the general depth it is today. Therefore, even though there was abundant quartz cementation,

Table 1. Data used to calculate IGV's. IGV is the sum of porosity plus quartz cementation.

Well Name	Depth (ft)	IGV% (SEM-CL analysis)	IGV% (Thin-section point-count analysis)	Porosity (%)	SEM-CL quartz cementation (%)	Point-count quartz cementation (%)
Cities Service No. B2 Killingsworth	3636	39.0	21.7	15.7	23.3	6.0
ARCO No. 18 Griffin	3641	40.3	25.4	11.8	28.5	13.6
ARCO No. 18 Griffin	3641	41.0	26.6	13.0	28	13.6
ARCO No. 18 Griffin	3627	42.2	32.9	16.6	25.6	16.3
ARCO No. 68 Kinney	3665	42.6	34.9	17.1	25.5	17.8
ARCO No. 18 Griffin	3665	44.4		14.6	29.8	N/A
Mean		41.6	28.3	14.8	26.8	13.6

a large number of intergranular pores survived burial diagenesis, leaving a network of well-connected pores to form high-quality Woodbine reservoirs.

The SEM-CL image analysis revealed two stages of quartz cementation (Figs. 7C-7F). The first stage in contact with quartz framework grains is red in CL; the second stage is blue in CL (Fig. 7E). The distribution and morphology of the first-stage quartz overgrowth suggests it is not related to a relict overgrowth from the source area. Figure 7, an SEM-CL image, shows complex crystal growth patterns of chevrons oriented away from the grain. The second stage of quartz overgrowths is volumetrically more abundant than the first stage. On many grains, the crystal terminations are euhedral (Fig. 12A), while on other grains the quartz overgrowths are poorly developed (Fig. 12B).

Carbonate Cementation and Other Cements

Only a few wells show rare to minor carbonate cementation. In the Cities Service No. 2B Killingsworth well, some poikilotopic calcite (Fig. 13A) was precipitated in the soil zone at the upper erosional surface of the Woodbine section. The absence of quartz overgrowths within this poikilotopic calcite indicates the calcite cement was precipitated before burial. In a few samples, the poikilotopic calcite reduced porosity, but it is not a significant factor for reservoir quality of Woodbine reservoirs.

Siderite crystals (Figs. 13B-13D), which are loafish (Fig. 13B), occur in just a few wells and are less than 0.5 percent by volume. Fluid chemistry must have been variable during some of the siderite precipitation since many of the crystals start out as siderite, followed by calcite, and then again by siderite (Figs. 13C and 13D). Commonly, the calcite layer is dissolved, forming a porous band within the crystal.

Another diagenetic product is rare chlorite clay (Fig. 13E) noted in one sample, which was recognized using SEM microscopy. The chlorite appears to coat grains, but it may be grain replacement. In Figure 7F, the chlorite appears to have formed after quartz overgrowths, which supports it being a later replacement product of unstable grains.

One sample (ARCO No. 9X Strickland; 3584.9 ft) has patches of pyrite that may have formed in the soil zone (Fig. 13F). The pyrite patches encompass numerous floating grains, indicating very shallow precipitation. The IGV, based on point counts (200 points), is 52 percent.

PORES AND PORE NETWORKS

Three types of pores are observed in the East Texas Field Woodbine sandstones: (1) primary intergranular pores, (2) secondary dissolution pores, and (3) micropores. The amount of each pore type varies among the three rock types: (1) matrix-free

sandstone, (2) matrix-rich sandstone, and (3) sandy conglomerate.

Matrix-Free Sandstone Pores

In matrix-free sandstones, primary intergranular pores are dominant (Figs. 7A and 12). These pores are partly occluded by quartz overgrowths. Only in a few thin sections are other cements present above trace amounts. Even though the volume of quartz overgrowths can be as high as 28 percent, porosities greater than 30 percent were preserved. Some secondary dissolution pores are present, but are generally less than 1 percent in volume (Figs. 8A-8D). These secondary pores are related to dissolved feldspars and volcanic rock fragments. Remnants of the partly dissolved grains are still evident (Figs. 8B-8D). Some of the feldspars and volcanic rock fragments may have been totally dissolved, creating oversized intergranular pores. However, because of the generally large pore size of primary intergranular pores, these dissolution-related oversized pores would be difficult to document and are also considered to be rare in the samples observed. Micropores occur in chert grains and in partly dissolved feldspars and volcanic rock fragments; however, these grains generally make up less than 0.5 percent by volume.

The pore network of the matrix-free sandstones is composed dominantly of well-connected intergranular pores. Very minor secondary dissolution and micropores are present but do not contribute to the effective pore network.

Matrix-Rich Sandstone Pores

The matrix-rich sandstones contain moderate porosity but generally very low permeability. Thin-section analysis reveals that macroscale, secondary dissolution pores (Fig. 9A), and possibly some partly mud-filled interparticle pores, exist. The dissolution pores are dissolved, isolated feldspars and volcanic rock fragments. SEM microscopy demonstrates that there are abundant nano- to micropores in the muddy matrix between and within clay platelets (see Loucks et al. [2012] for discussion of classification of nano- to micropore mud-dominated rocks) (Figs. 9E and 9F). The abundant fine-scale pores associated with clay platelets are related to a rigid framework of sand grains that produce compaction shadows within the framework. The clay platelets show bending but not severe compaction. The bending of the platelets created intraparticle pores through mechanical deformation, causing clay layers within the platelets to separate (Fig. 9F). Another less-common pore type revealed by SEM microscopy is partially-dissolved pyrite crystals or framboids.

The pore network in the matrix-rich sandstones is dominated by nano- to micropores between and within clay platelets in compaction shadows. Some secondary dissolution pores exist, but

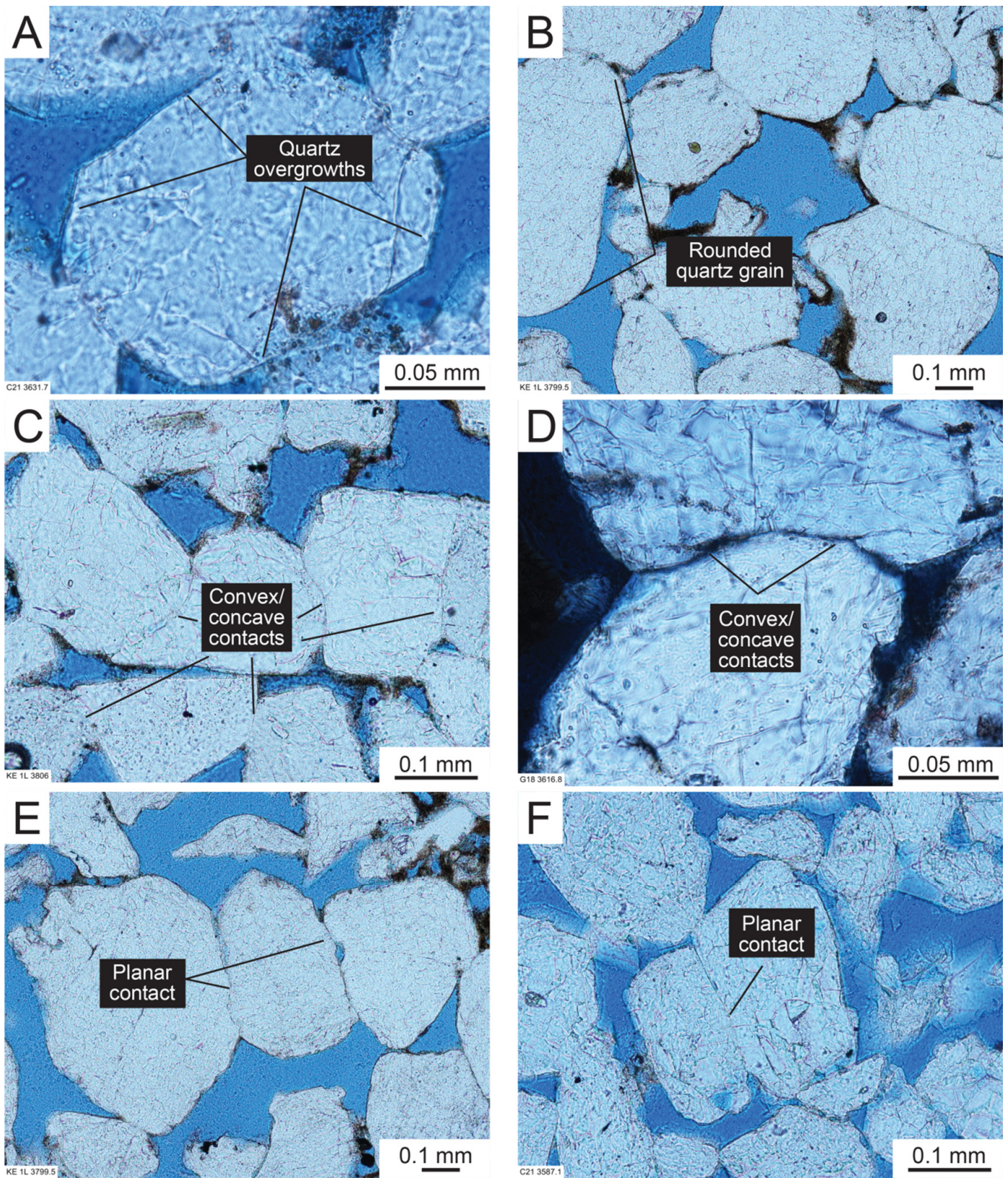


Figure 12. Quartz overgrowth cementation. (A) Quartz overgrowth with well-developed crystal faces (ARCO No. C21 Pinkston; 3631 ft). (B) Quartz sandstone lightly cemented by quartz overgrowths (Key No. 1 Lawson; 3799 ft). Some of the grains have no overgrowth and are still rounded. Dark material may be drilling mud. (C) Quartz overgrowths indicated by convex/concave contacts (Key No. 1 Lawson; 3806 ft). (D) Quartz overgrowths indicated by convex/concave contacts (ARCO No. 1 Griffin; 3616 ft). Photomicrograph taken under cross-polarized light. (E) Quartz overgrowths indicated by planar boundaries (Key No. 1 Lawson; 3799 ft). (F) Planar boundary between quartz grains suggests quartz overgrowth cementation competition (ARCO No. C21 Pinkston; 3587 ft).

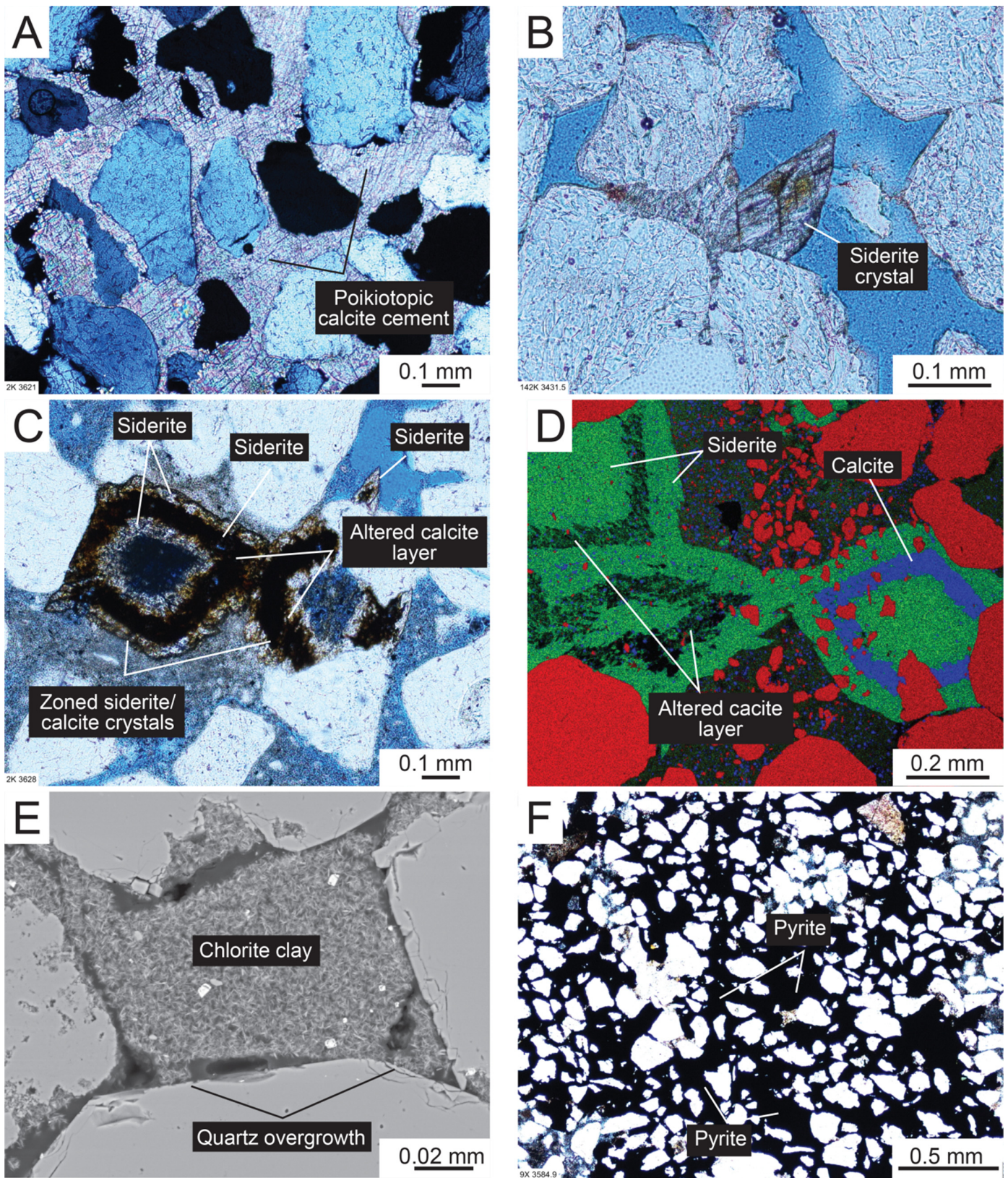


Figure 13. Carbonate and other cements. (A) Poikiloblastic calcite in a noncompacted fabric (Cities Service No. B2 Killingsworth; 3621 ft). (B) Loafish crystals of siderite cement (ARCO No. B142 King; 3131 ft). (C) Zoned siderite/calcite crystals with the middle calcite layer altered (Cities Service No. B2 Killingsworth; 3628 ft). (D) False-color EDS map of zoned siderite/calcite crystals with some of the calcite layers altered (Cities Service No. B2 Killingsworth; 3637 ft). Si is red, Fe is green, and Ca is blue; therefore, quartz is red, siderite is green, and calcite is blue. (E) SEM image showing chlorite clay-grain replacement and cement (Cities Service No. B2 Killingsworth; 3637 ft). (F) Large patch of pyrite cementation with an IGv of 52% (ARCO No. 9X Strickland; 3584 ft).

they are isolated from each other. The nano- to micropore network appears to be well connected, but the small pore throats (discussed in section on reservoir quality) produce low permeability.

Sandy Conglomerate Pores

The sandy conglomerates are a mixture of sand, granules, and pebbles. Sand is the most abundant component, and primary intergranular pores between the sand grains dominate the pore network (Figs. 10C and 10E). Quartz overgrowths, as well as isolated siderite crystals, occlude some of these pores. Also, because the intergranular pore network is so porous, drilling mud filtered into the pores (Fig. 10E). This drilling mud appears as very fine material, commonly forming a halo around the pore as the result of the mud drying out. This artificially induced material plugs pore throats, thus affecting the MICP analysis.

Most of the granules and pebbles are chert clasts that formed from chertification of dolomitic limestones. The chert contains common micro- and macropores (Figs. 10C and 10F). Many of the macropores are dissolved dolomite rhombs (Fig. 10F) or sponge spicules connected by micropores. The porous chert clasts do not add to the effective pore system, but because of their microporous character, they can hold irreducible water and affect resistivity-based saturation calculations from wireline logs. This factor may make the lithofacies appear to have high water content, but the water may not be produced along with the oil.

Rare secondary dissolution pores occur in scattered feldspar grains and unidentifiable grains; a dissolution zone also occurs with siderite crystals where the calcite layer was dissolved (Figs. 13C and 13D). The secondary dissolution pores are rare and isolated, and therefore do not contribute to effective porosity. The pore networks in the sandy conglomerates are similar to the matrix-free sandstones except that more nano- to micropores are present within the chert clasts.

Organic-Matter Pores

Another interesting pore type, although rare, is the organic-matter-related pore (OM pore). OM pores occur in two forms: (1) primary inherited in wood fragments (Fig. 14A), and (2) depositional kerogen (Fig. 14B). The Woodbine sandstone contains wood fragments that show elongated pores parallel to each other; fragments are approximately 200 μm long and 25 μm wide. The smallest pores, in the nanometer range and circular, are interpreted to be related to the cellular structure of the original organic matter.

Some less-identifiable kerogen of small size is present between clay platelets (Fig. 14B) and has numerous bubble-like pores, with some aligned. Sizes of visible pores, based on SEM analysis, range from 10 to 100 nm. The pores are the result of thermal maturation of kerogen (Loucks et al., 2009; Loucks and Reed, 2014). The alignment of nanopores suggests that the pores are controlled by the original internal structure of the kerogen (Loucks and Reed, 2014).

RESERVOIR QUALITY

Porosity and Permeability Data and Analysis

Reservoir quality in the East Texas Field sandstones is high but variable (Figs. 15 and 16). The major factor controlling reservoir quality is the presence or absence of matrix within the sandstone, which is a function of depositional processes, as discussed below. The analysis of a core porosity and permeability data set provided by the East Texas Engineering Association from 35 wells (738 porosity values and 582 permeability values collected from 1935 to 2005) (Fig. 15) shows a calculated mean porosity of 20.9 percent and a mean permeability of 1383 md (geometric mean of 102 md). This analysis included sandstone

samples both with and without matrix. If samples with matrix (a general correlation with samples having less than 30-md permeability) are eliminated from the analysis, a mean porosity of 26.0 percent and a mean permeability of 1987 md (geometric mean of 1070 md) are calculated. The range of porosity is from 3 to 38 percent, and the range of permeability is from less than 0.01 to over 10,000 md. The environmental parameters used to calculate these values are not known, nor whether the permeability value has a Klinkenberg correction. These data demonstrate the high reservoir, but variable quality of the Woodbine sandstones in the East Texas Field.

Core Laboratories in Houston analyzed 49 additional core-plug samples. Samples with and without matrix were selected for analysis, and the samples were run at confining pressures of 800 and 2000 psi. These samples allow the differentiation of reservoir quality of sandstone with and without matrix (Fig. 16).

Matrix-Free Sandstones

Thirty-two matrix-free sandstones under a confining pressure of 2000 psi give a mean porosity of 24.0 percent and a mean permeability of 745 md (geometric mean of 410 md) (Fig. 16). The range in porosity is 4.7 to 37.4 percent, and the range in permeability is 7.51 to 2320 md. Because these matrix-free sandstones were analyzed under reservoir conditions, their mean values are expected to be lower than the mean of sandstones in the larger dataset discussed earlier.

Matrix-Rich Sandstones

Sixteen matrix-rich sandstones analyzed under a confining pressure of 2000 psi give a mean porosity of 14.8% and a mean permeability of 5.1 md (geometric mean of 0.88 md) (Fig. 16). The range of porosity is 7.8 to 25.5 percent, and the range of permeability is 0.001 to 37.4 md. From Figure 16, it is obvious that there are two populations of matrix-rich sandstones. One group plots with the matrix-free sandstones, which have a minor amount of matrix. The other group of matrix-rich sandstones have poor to fair porosities (up to 18 percent) but very poor permeabilities (less than 0.2 md). The high porosities of this second group are related to abundant nano- to micropores between and within clay platelets (Figs. 9E and 9F). Therefore, porosities as high as 18 percent calculated from wireline logs can have permeabilities less than 0.2 md.

Depositional Environment Control on Reservoir Quality

Depositional environment has a strong overriding influence on reservoir quality because the physical processes within the depositional environment have an effect on whether matrix-rich or matrix-free sandstones are deposited. Within each depositional system is a variety of lithofacies, some matrix free and some matrix rich. Figure 17 is a plot of mean porosity versus mean permeability separated by each depositional system. The plot shows that all the sandstone lithofacies have good to excellent reservoir quality as a whole. These mean values average both matrix-free and matrix-poor sandstones. Therefore, the conclusion from this plot is that in any depositional system there will be ample high-quality reservoirs to ensure success in any well.

Mercury-Injection Capillary-Pressure (MICP) Data and Analysis

MICP analysis provides more detailed insight into controls on permeability than do core-plug-permeability measurements alone (Pittman, 1992). MICP measurements can be converted to pore-throat size, which is one of the basic controls on permeability. Five sandstone samples were selected for MICP analysis that

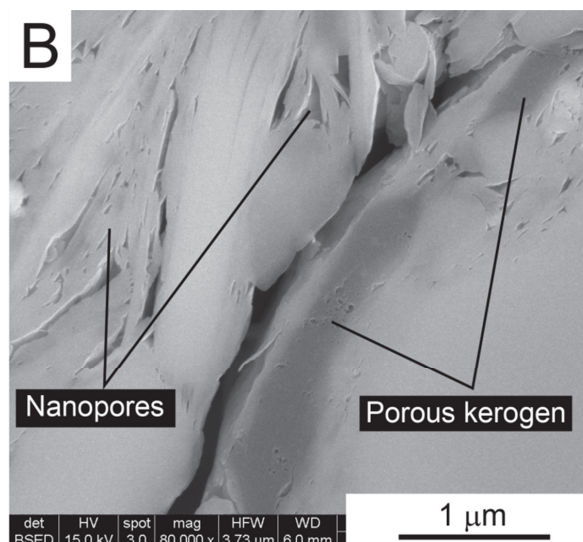
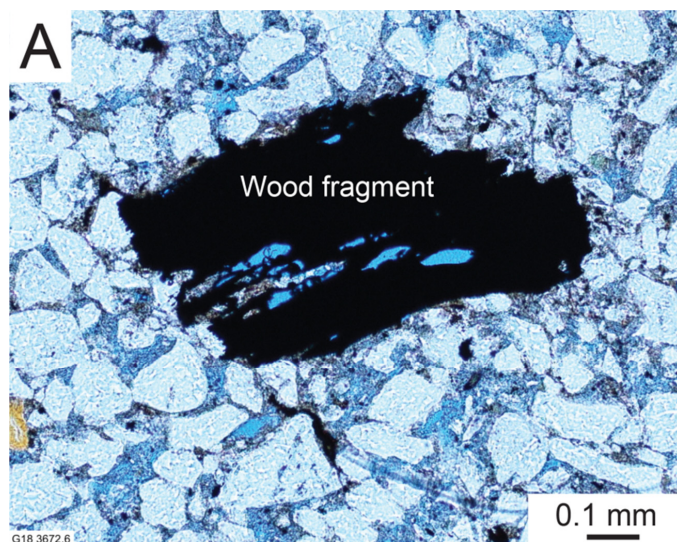


Figure 14. Organic-matter pores. (A) Wood fragment with original pores (ARCO No. 18 Griffin; 3672 ft). (B) SEM image showing kerogen with organic-matter, bubble-like pores interlaminated with porous clay platelets (ARCO No. 18 Griffin; 3628 ft).

covered a broad range in permeability (0.15 to 2430 md) (Figs. 18–20). Two sandstone samples were very fine- to fine grained, with one containing abundant matrix (Fig. 18A) and the other containing rare matrix (Fig. 18B). The other three samples are fine- to medium-grained, matrix-free sandstones (Figs. 18C–18E).

Figure 19 shows that the three high-quality sandstones have entry pressures of less than 6 psi and mean pore-throat sizes between 5 and 15 μm , whereas one matrix-rich sandstone has an entry pressure of 82 psi, with the sizes of pore throats poorly sorted and ranging between 0.01 and 1 μm in diameter (Fig. 20). Figure 21 supports the concept that mean pore-throat radius and permeability are closely related. This log-log plot also displays permeability versus P35, which is the general pore-throat size that is considered to most control permeability (Kolodzie, 1980). Both pore-throat values show a similar strong relationship to permeability. In the following section, each of the five MICP analyses are examined.

(1) Sun No. 1 Temple (5137 ft; Fig. 18A)

This is a very poorly-sorted, very fine- to fine-grained, matrix-rich sandstone with a porosity of 13.7 percent and a permeability of 0.15 md. It was deposited as a highstand crevasse splay (Ambrose and Hentz, 2010). It is interpreted to have been altered by soil processes (Ambrose and Hentz, 2010). Mean pore-throat radius is 0.15 μm , with only a few pore radii larger than 1 μm (Fig. 20), well into the micropore range (pore-throat radii less than 0.5 μm). Pore throats are poorly sorted (Fig. 20). The MICP curve (Fig. 21) shows a high entry pressure of 82 psi, indicating a relatively tight sandstone. The shape of the curve reflects the wide range and poor sorting of the pore-throat radii.

(2) ARCO No. 68 Kinney (3630 ft; Fig. 18B)

The thin section of this sandstone show the sample to be a moderately sorted, very fine- to fine-grained, matrix-free sandstone. It was deposited as a highstand crevasse splay (Ambrose and Hentz, 2010). It may have traces of matrix. The sample has a porosity of 23.7 percent and a permeability of 99.2 md. Most pore-throat radii are in the 4–7 μm range, with a tail out to 0.01 μm (Fig. 20). Mean pore-throat radius is 2.67 μm . According to the MICP curve (Fig. 19), the larger pore throats are well sorted, but the finer pore throats are very poorly sorted.

(3) Shell No. 55 Watson (3630 ft; Fig. 18C)

This is a moderately-sorted, fine- to medium-grained, matrix-free sandstone. It was deposited in a highstand distributary channel (Ambrose and Hentz, 2010). It has a porosity of 28.6 percent and a permeability of 862 md. Mean pore-throat size is 10.6 μm , with a tail out to 0.02 μm (Fig. 20). Figure 20 shows that a narrow pore-size range dominates. The MICP curve shows fairly well-sorted pore-throat sizes (nearly flat up to 55 percent mercury saturation) (Fig. 19).

(4) ARCO No. 69 Kinney (3660 ft; Fig. 18D)

This is a well-sorted, fine- to medium-grained, matrix-free sandstone. It was deposited as a highstand crevasse splay (Ambrose and Hentz, 2010). It has a porosity of 27.5 percent and a permeability of 1680 md. Mean pore-throat size is 14.3 μm (Fig. 20). Figure 20 shows that one pore-size range dominates. These pore throats are well into the macropore throat-size range (Fig. 20). The MICP curve shows very well-sorted pore-throat sizes (nearly flat up to 70 percent mercury saturation) (Fig. 19).

(5) ARCO No. 18 Griffin (3578 ft; Fig. 18E)

This is a well-sorted, fine- to medium-grained, matrix-free sandstone. It was deposited in a highstand distributary channel (Ambrose and Hentz, 2010). It has a porosity of 29.3 percent and a permeability of 2430 md. Mean pore-throat size is 14.3 μm (Fig. 20), the same as the ARCO No. 69 Kinney sandstone sample above. Figure 20 shows that one pore-size range dominates. These pore throats are well into the macropore throat-size range. The MICP curve shows very well-sorted pore-throat sizes (nearly flat up to 75 percent mercury saturation) (Fig. 19).

CONCLUSIONS

The Woodbine Group in the East Texas Field is an excellent oil reservoir in part because of its stable quartz-framework mineralogy and early quartz-overgrowth cementation. Quartz-framework grains are mechanically and chemically stable, and the relatively shallow onset of quartz-overgrowth precipitation precluded extensive compaction. Many of the matrix-free sandstones survived burial and diagenesis with an excellent intact primary intergranular pore network that is characterized by a

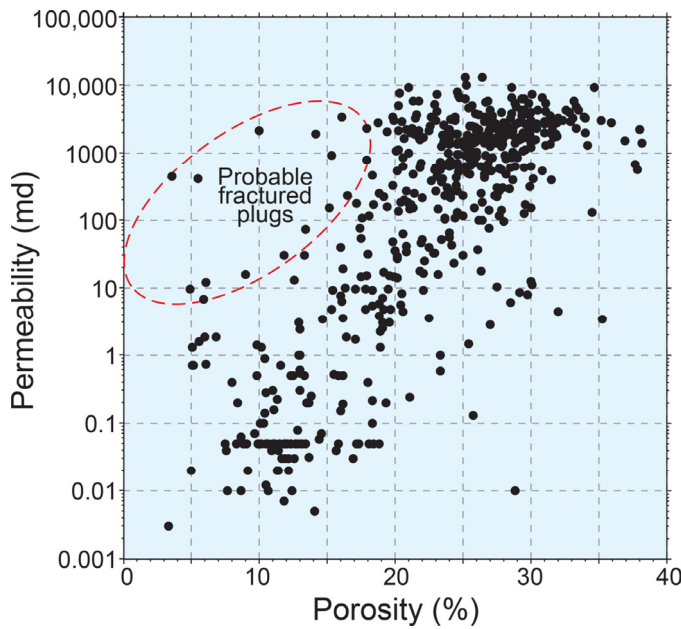


Figure 15. Porosity versus permeability scatter plot for Woodbine sandstone samples from the East Texas Field (modified after Loucks, 2010). Dates of sample analyses range from 1935 to 2005 and both air and Klinkenberg permeabilities are presented in the plot.

mean porosity of approximately 26.0 percent and a mean permeability of approximately 2000 md. The matrix-free sandstones have large mean pore throats well into the macropore throat range (pore-throat radii as high as 14.3 μm). The abundance of matrix is a dominant factor in separating poor-quality from high-quality sandstone. Most matrix-rich sandstones have permeabilities less than 0.2 md, whereas most matrix-free sandstones have permeabilities greater than 100 md. The relationship of matrix-free sandstones and high-quality reservoirs is important to understand. There is little risk of not encountering reservoir-quality sandstone in the East Texas Field if sandstone isopachs are used to map out the depositional systems.

ACKNOWLEDGMENTS

The authors would like to acknowledge reviews by Earle McBride and David Hull. Shirley Dutton and Kitty Milliken helped clarify a number of concepts presented in this study. We express our appreciation to Stephanie Jones for editing the manuscript. Patrick Smith ion-milled samples for this study. The East Texas Engineering Association shared porosity and permeability analyses. The research was funded by STARR (State of Texas Advanced Oil and Gas Resource Recovery Program) at the Bureau of Economic Geology, University of Texas at Austin. Publication was authorized by the Director, Bureau of Economic Geology, Jackson School of Geosciences, University of Texas at Austin.

REFERENCES CITED

Ambrose, W. A., and T. F. Hentz, 2010, Depositional systems and facies variability in highstand fluvial-dominated deltaic and lowstand valley-fill systems in the Lower Cretaceous (Cenomanian) Woodbine Group, East Texas Field, in T. F. Hentz, ed., Sequence stratigraphy, deposition facies, and reservoir attributes of the Upper Cretaceous Woodbine Group, East Texas Field: Texas Bureau of Economic Geology Report of Investigations 274, Austin, 114 p.
 Ambrose, W. A., T. F. Hentz, F. Bonnafé, R. G. Loucks, L. F. Brown, Jr., F. P. Wang, and E. C. Potter, 2009, Sequence strati-

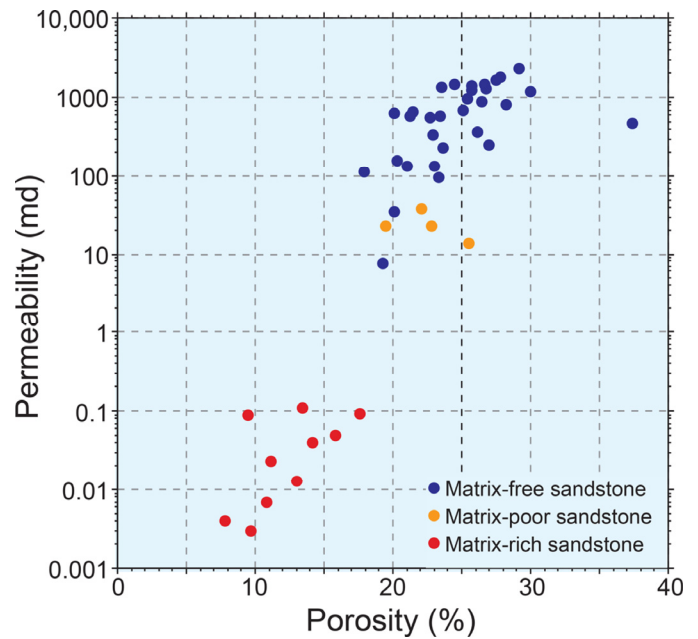


Figure 16. Porosity versus permeability scatter plot for Woodbine sandstones under in situ conditions of 2000 psi. Klinkenberg correction for permeabilities.

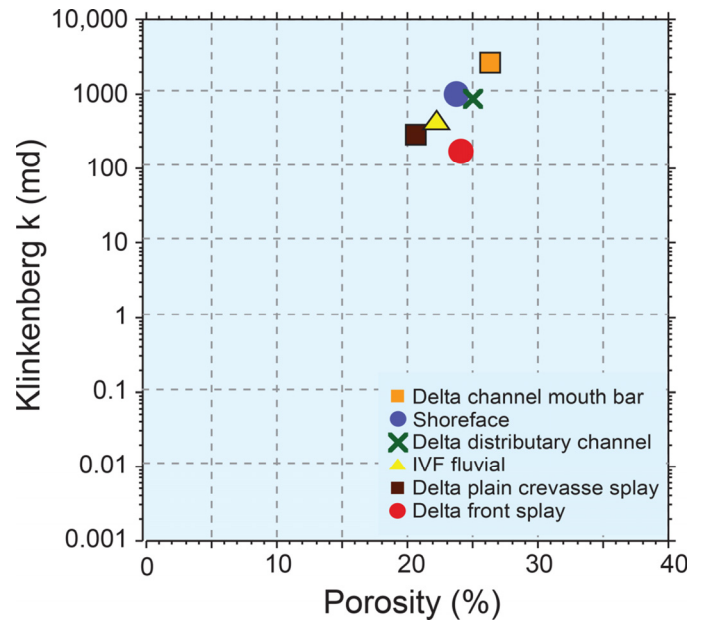


Figure 17. Mean porosity versus mean Klinkenberg permeability (2000 psi) separated by depositional facies.

graphic controls on complex reservoir architecture of highstand fluvial-dominated deltaic and lowstand valley-fill deposits in the Upper Cretaceous (Cenomanian) Woodbine Group, East Texas Field: Regional and local perspectives: American Association of Petroleum Geologists Bulletin, v. 93, p. 231-269.

Atkins, J. E., and E. F. McBride, 1992, Porosity and packing of Holocene river, dune, and beach sands: American Association of Petroleum Geologists Bulletin, v. 76, p. 339-355.
 Beall, A. O., Jr., 1964, Fabric and mineralogy of Woodbine sediments, east-central Texas: Ph.D. Dissertation, Stanford University, California, 171 p.
 Cotera, A. S., Jr., 1956, Petrology of the Cretaceous Woodbine sand in northeast Texas: M.S. Thesis, University of Texas at Austin, 152 p.

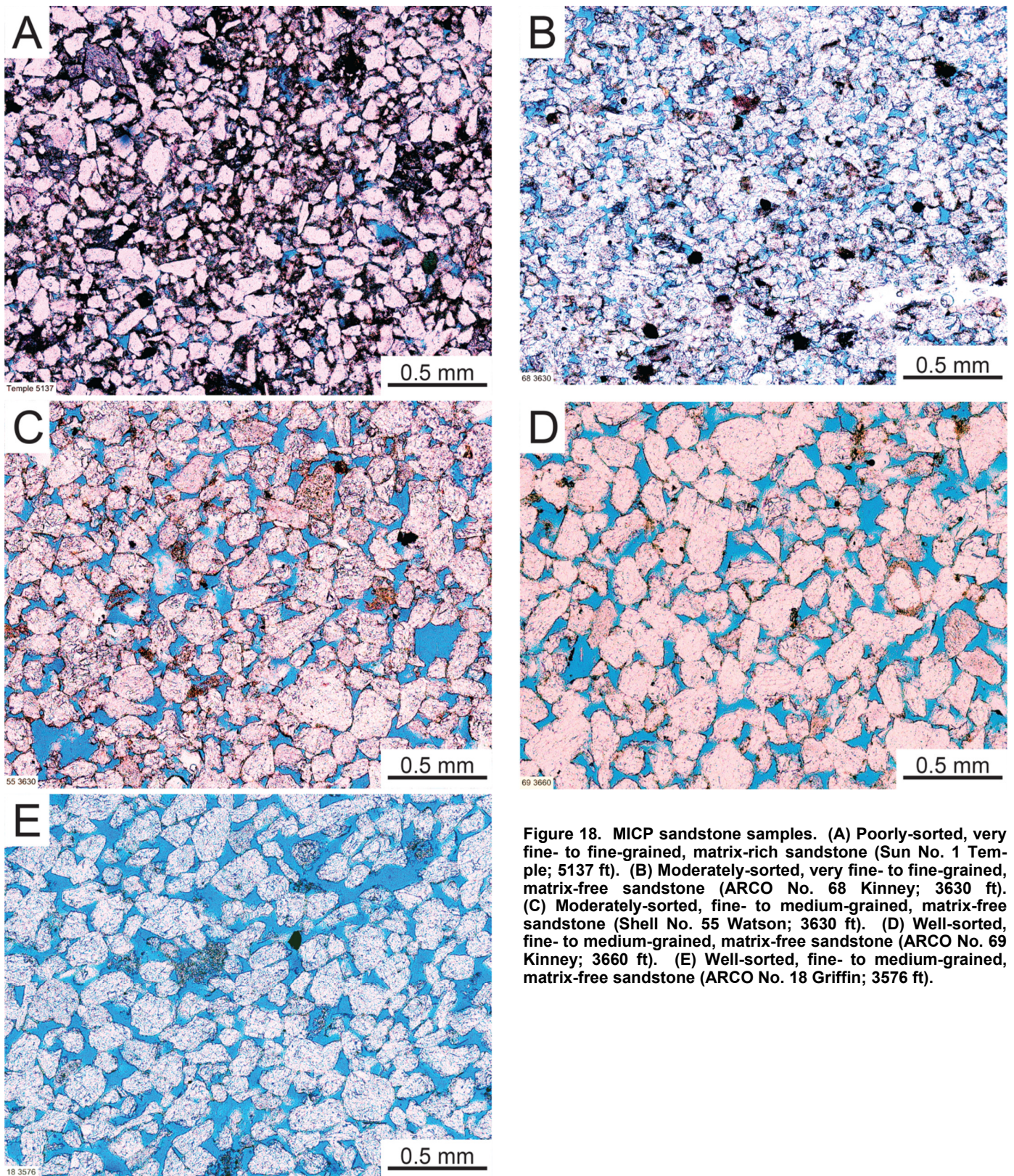


Figure 18. MICP sandstone samples. (A) Poorly-sorted, very fine- to fine-grained, matrix-rich sandstone (Sun No. 1 Temple; 5137 ft). (B) Moderately-sorted, very fine- to fine-grained, matrix-free sandstone (ARCO No. 68 Kinney; 3630 ft). (C) Moderately-sorted, fine- to medium-grained, matrix-free sandstone (Shell No. 55 Watson; 3630 ft). (D) Well-sorted, fine- to medium-grained, matrix-free sandstone (ARCO No. 69 Kinney; 3660 ft). (E) Well-sorted, fine- to medium-grained, matrix-free sandstone (ARCO No. 18 Griffin; 3576 ft).

Dutton, S. P., and T. N. Diggs, 1990, History of quartz cementation in the Lower Cretaceous Travis Peak Formation, East Texas: *Journal of Sedimentary Research*, v. 60, p. 191–202.
 Dutton, S. P., and L. S. Land, 1988, Cementation and burial history of a low-permeability quartzarenite, Lower Cretaceous Travis Peak Formation, East Texas: *Geological Society of America Bulletin*, v. 100, p. 1271–1282.

Ehrenberg, S. N., 1995, Measuring sandstone compaction from modal analyses of thin sections: How to do it and what the results mean: *Journal of Sedimentary Research*, v. 65A, p. 369–379.
 Folk, R. L., 1974, *Petrology of sedimentary rocks*: Hemphill, Austin, Texas, 182 p.
 Halbouty, M. T., 1991, East Texas Field—U. S. A., East Texas Basin, Texas, in N. H. Foster and E. A. Beaumont, eds., *Strati-*

graphic traps II: American Association of Petroleum Geologists Treatise of Petroleum Geology, Atlas of Oil and Gas Fields, Tulsa, Oklahoma, p. 189–203.

Hentz, T. F., ed., 2010, Sequence stratigraphy, deposition facies, and reservoir attributes of the Upper Cretaceous Woodbine Group, East Texas Field: Texas Bureau of Economic Geology Report of Investigations 274, Austin, 114 p.

Hentz, T. F., and F. Bonnaffé, 2010, Sequence stratigraphy of the Upper Cretaceous (Cenomanian) Woodbine Group: Chronostratigraphic integration of the East Texas Basin and East Texas Field, in T. F. Hentz, ed., Sequence stratigraphy, deposition facies, and reservoir attributes of the Upper Cretaceous Woodbine Group, East Texas Field: Texas Bureau of Economic Geology Report of Investigations 274, Austin, p. 1–16.

Houseknecht, D. W., 1987, Assessing the relative importance of compaction processes and cementation to reduction of porosity in sandstones: American Association of Petroleum Geologists Bulletin, v. 71, p. 633–642.

Kearsley, A., and P. Wright, 1988, Geological applications of scanning electron cathodoluminescence imagery: Microscopy and Analysis, September 1988 issue, p. 49–51.

Kolodzie, S., Jr., 1980, Analysis of pore throat size and use of the Waxman-Smiths equation to determine OOIP in Spindle Field, Colorado: Society of Petroleum Engineers Paper 9382, Richardson, Texas, 10 p.

Loucks, R. G., 2010, Petrographic controls on reservoir quality of the Upper Cretaceous Woodbine Group, East Texas Field, in T. F. Hentz, ed., Sequence stratigraphy, deposition facies, and reservoir attributes of the Upper Cretaceous Woodbine Group, East Texas Field: Texas Bureau of Economic Geology Report of Investigations 274, Austin, p. 83–93.

Loucks, R. G., and R. M. Reed, 2014, Scanning-electron-microscope petrographic evidence for distinguishing organic-matter pores associated with depositional organic matter versus migrated organic matter in mudrocks: Gulf Coast Association of Geological Societies Journal, v. 3, p. 51–60.

Loucks, R. G., R. M. Reed, S. C. Ruppel, and U. Hammes, 2012, Spectrum of pore types and networks in mudrocks and a descriptive classification for matrix-related mudrock pores: American Association of Petroleum Geologists Bulletin, v. 96, p. 1071–1098.

Loucks, R. G., R. M. Reed, S. C. Ruppel, and D. M. Jarvie, 2009, Morphology, genesis, and distribution of nanometer-scale pores in siliceous mudstones of the Mississippian Barnett Shale: Journal of Sedimentary Research, v. 79, p. 848–861.

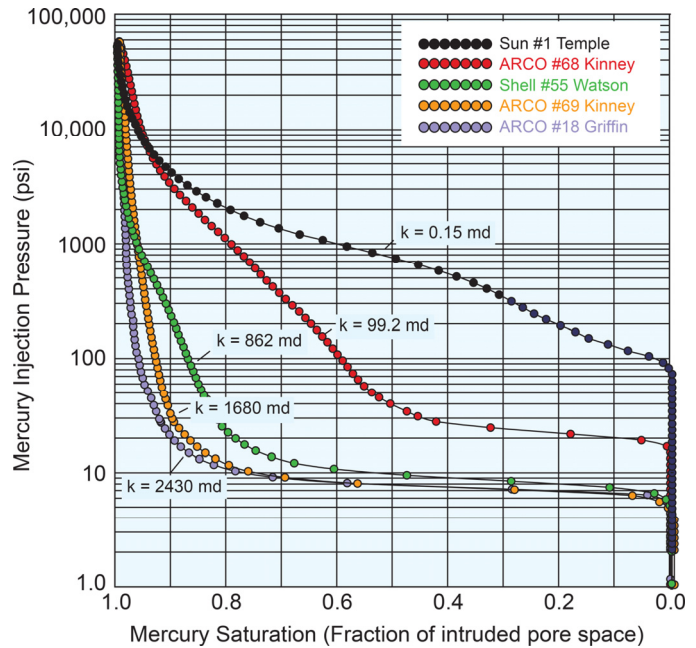


Figure 19. MICP curves for selected Woodbine sandstones.

Lundegard, P. D., 1992, Sandstone porosity loss—A “big picture” view of the importance of compaction: Journal of Sedimentary Petrology, v. 62, p. 250–260.

Oliver, W. B., 1971, Depositional systems in the Woodbine Formation (Upper Cretaceous), northeast Texas: Texas Bureau of Economic Geology Report of Investigations 73, Austin, 28 p.

Paxton, S. T., J. O. Szabo, J. M. Ajdukiewicz, and R. R. Klimentidis, 2002, Construction of an intergranular volume compaction curve for evaluating and predicting compaction and porosity loss in rigid-grain sandstone reservoirs: American Association of Petroleum Geologists Bulletin, v. 86., p. 2047–2067.

Pittman, E. D., 1992, Relationship of porosity and permeability to various parameters derived from mercury injection-capillary pressure curves for sandstone: American Association of Petroleum Geologists Bulletin, v. 76, p. 191–198.

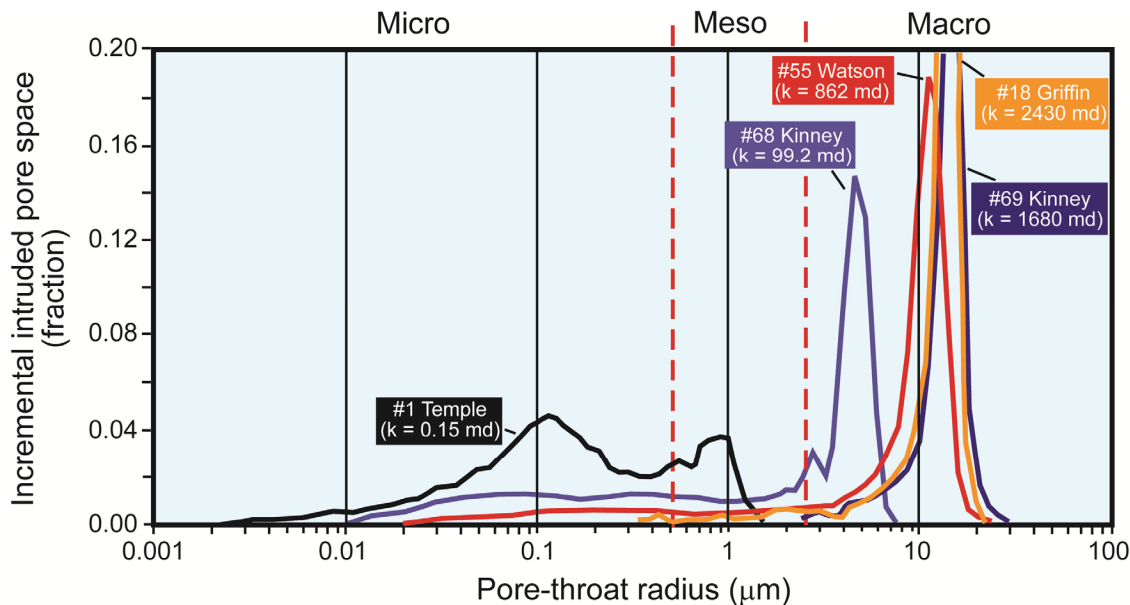


Figure 20. Pore-throat-radius frequency curves calculated from MICP analysis.

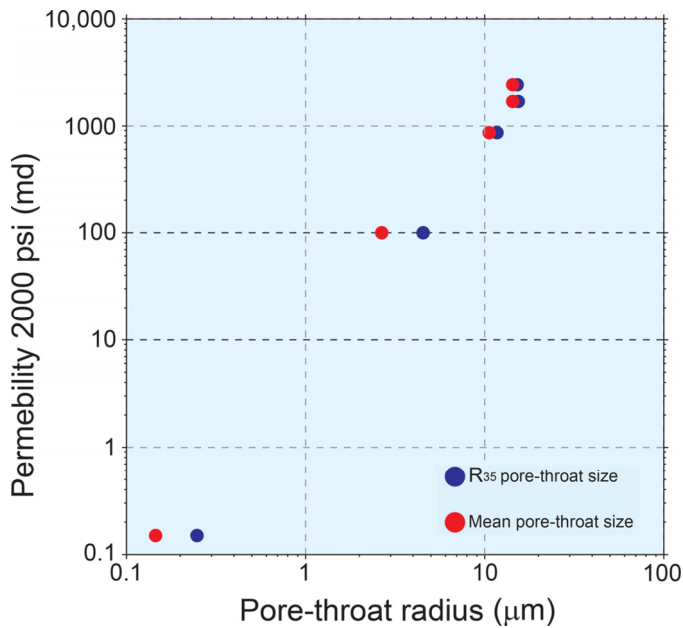


Figure 21. Log-log scattergram of mean pore-throat radius and R35 pore-throat radius versus permeability.

Ross, C. S., H. D. Miser, and L. W. Stephenson, 1929, Water-laid rocks of early Upper Cretaceous age in southwestern Arkansas, southeastern Oklahoma, and northeastern Texas: U.S. Geological Survey Professional Paper 154F, p. 175–202.

Sims, D. E., 1982, Environment facies of the Woodbine sandstone, Wood County, Texas: B.S. Thesis, Baylor University, Waco, Texas, 68 p.

Wang, F. P., W. A. Ambrose, T. F. Hentz, F. Bonnaffé, R. G. Loucks, 2008, Engineering and geologic characterization of giant East Texas Oil Field: Northern and southern pilot studies: Society of Petroleum Engineers 115683, Richardson, Texas, 16 p.